UCRL-ID-131489

Multiscale Thermohydrologic Model Sensitivity Analysis

by

Thomas A. Buscheck, James Gansemer, Truc H. De Lorenzo, John J. Nitao, and Ronald J. Shaffer

July 31, 1998

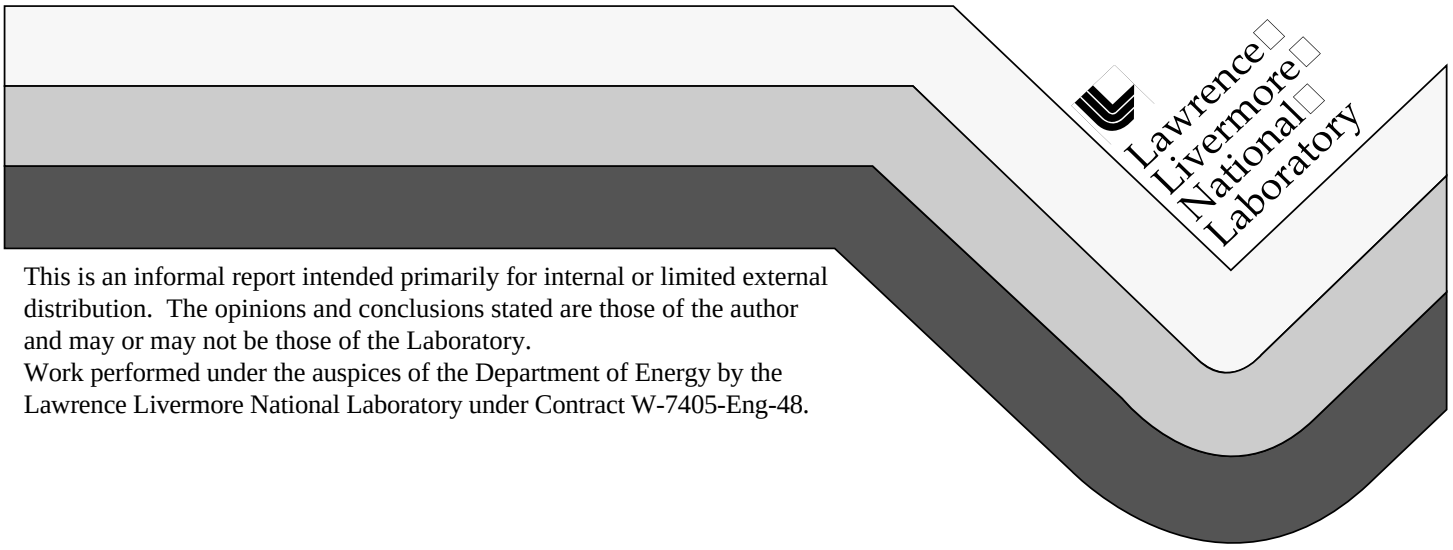

Work performed under the auspices of the Department of Energy by the Lawrence Livermore National Laboratory under Contract W-7405-Eng-48.

UCRL-ID-131489

Multiscale Thermohydrologic Model Sensitivity Analysis

by

**Thomas A. Buscheck, James Gansemer,
Truc H. De Lorenzo, John J. Nitao, and Ronald J. Shaffer**

SP4CK5M4

July 1998

Lawrence Livermore National Laboratory

Livermore, California

Contents

Tables

Figures

Abbreviations and Acronyms

1-D	one-dimensional
2-D	two-dimensional
3-D	three-dimensional
AML	areal mass loading
APD	areal power density
BWR	boiling-water reactor
CCDF	complementary cumulative density function
CSNF	commercial spent nuclear fuel
DDT	discrete-heat-source, drift-scale thermal conduction
DDTH	discrete-heat-source, drift-scale thermohydrologic
DFM	discrete-fracture method
DHLW	defense high-level waste
DKM	dual-permeability method
DMTH	discrete-heat-source, mountain-scale thermohydrologic
DOE	U.S. Department of Energy
EBS	engineered barrier system
ECM	equivalent-continuum method
FMX	fracture–matrix interaction
LBNL	Lawrence Berkeley National Laboratory
LBT	Large-Block Test
LDTH	line-averaged-heat-source, drift-scale thermohydrologic
LLNL	Lawrence Livermore National Laboratory
LML	lineal mass loading
LMTH	line-averaged-heat-source, mountain-scale thermohydrologic
NF/AZ	near field and altered zone
NFE	near-field environment
NUFT	Nonisothermal Unsaturated-Saturated Flow and Transport
PWR	pressurized water reactor
SDT	smeared-heat-source, drift-scale thermal-conduction
SDTH	smeared-heat-source, drift-scale thermohydrologic
SHT	Single-Heater Test
SMT	smeared-heat-source, mountain-scale thermal-conduction
SNF	spent nuclear fuel
SZ	saturated zone

TH	thermohydrologic
TSPA–VA	Total System Performance Assessment–Viability Assessment
UZ	unsaturated zone
WP	waste package
YM	Yucca Mountain

Acknowledgments

The authors gratefully acknowledge the review of Wunan Lin. This report could not have been completed in such a timely manner without the editing of Karen L. Lew and Peter J. Gaughan, as well as the graphic-design support of Paul Harding.

1. Introduction

A multiscale, thermohydrologic (TH) modeling approach (or methodology) has been developed that integrates the results from one-dimensional (1-D), two-dimensional (2-D), and three-dimensional (3-D) drift-scale models and a 3-D mountain-scale model to calculate the near-field TH variables affecting the performance of the engineered barrier system (EBS) of the potential repository at Yucca Mountain. This information is required by Total System Performance Assessment—Viability Assessment (TSPA-VA) to assess waste-package (WP) corrosion, waste-form dissolution, and radionuclide transport in the EBS. This methodology is a computationally efficient, flexible means of determining EBS TH conditions; such determination would otherwise require millions of grid blocks if a brute-force numerical model were used. The methodology determines EBS TH conditions as a function of location within the repository and WP type.

Under ambient conditions, relative humidity *RH* is high and therefore corrosive. Decay heat from WPs results in a period of reduced *RH* in the EBS. The EBS TH model results are provided to PA as probability-density functions (or histograms) with respect to time to attain potentially corrosive *RH* conditions on WPs, and WP temperature when corrosive *RH* conditions are attained. The multiscale methodology captures the key factors affecting EBS TH conditions:

- Mountain-scale heat flow, including the effect of lateral heat loss at the repository edge
- Repository-scale variability in percolation flux
- WP-to-WP variability in heat output
- Matrix imbibition diffusivity of the local host-rock unit
- Fracture properties of the local host-rock unit
- Wet and dry thermal conductivity of the local host-rock unit
- Repository depth (or overburden thickness)

There are two major objectives of this study. The first is to examine the influence of hydrological parameter sets and infiltration-flux magnitude on near-field and EBS TH conditions. The hydrological parameters (also called properties) of key importance fall under the following categories:

- **Matrix parameters** that govern the matrix imbibition diffusivity (which is a measure of the magnitude of imbibition flux that rewets the dryout zone)
- **Fracture parameters** that govern the magnitude of capillary wicking in fractures; the key parameter of interest is the van Genuchten alpha parameter α_f for fractures, which is equivalent to the air-entry (or bubble-point) pressure
- **Nonequilibrium fracture-matrix interaction (FMX):** the FMX parameter for liquid-phase interaction accounts for channeling of flow as the liquid phase "fingers" through the fracture network

Comparisons are made between various parameter sets assumed by TSPA-VA as well as with alternative sets that have been developed (Hardin et al., 1998). The near-field/EBS variables that are examined include drift-wall temperature, drift-wall *RH*, WP temperature, WP *RH*, and liquid-phase flux 3 m above the drift.

For TSPA-VA (CRWMS M&O, 1998), TH conditions on WPs are binned according to the time for WPs to attain $RH = 85\%$, which is called $t(RH = 85\%)$. An RH of 85% was selected because it is assumed in TSPA-VA to be the critical RH for the initiation of atmospheric corrosion. A useful way to display the distribution of TH conditions on all WPs in the repository is to use a complementary cumulative density function (CCDF) of $t(RH = 85\%)$. For this study, all of the hydrologic parameter sets and infiltration-flux cases are compared with the use of CCDFs of $t(RH = 85\%)$.

The second major objective of this study is to compare the predicted EBS TH conditions from two different modeling approaches: the multiscale TH modeling approach used in this study and an east–west cross-sectional TH model developed at Lawrence Berkeley National Laboratory (LBNL) (Haukwa et al., 1998). Because the cross-sectional model does not predict in-drift TH conditions, and because RH and liquid-phase saturation data was not provided from that model, only the host-rock temperatures predicted by the respective modeling approaches are compared in this report.

Chapter 2 describes the numerical models and assumptions used in this study:

- The TH process models
- The NUFT numerical simulation code
- How the dual-permeability method was applied
- The assumed hydrostratigraphy and infiltration-flux distribution
- The thermal property set
- The various hydrologic parameter sets that were analyzed
- The drift-scale and mountain-scale submodels
- The thermal-loading representation
- The multiscale TH modeling methodology that integrates the results of the drift- and mountain-scale submodels.

Chapter 3 describes the results of the sensitivity study, and Chapter 4 presents a summary and conclusions.

2. Numerical Models and Assumptions

This chapter describes the numerical-simulation code that was used to run the thermohydrologic (TH) process models; the one-, two-, and three-dimensional (1-D, 2-D, and 3-D) TH process models, including their boundary conditions and assumptions; the multiscale TH modeling (and abstraction) methodology that integrates the results of the process models; and the various parameter sets and infiltration-flux maps that were modeled in this study.

2.1 Thermohydrologic Process Models

The multiscale TH modeling methodology (described in Section 2.2) requires the results from process models, including 1-, 2-, and 3-D drift-scale models and a 3-D mountain-scale model, to calculate the performance measures in the engineered barrier system(EBS) and the near-field environment (NFE).

2.1.1 NUFT Numerical Simulation Code

All of the TH-model calculations in this study used the Nonisothermal Unsaturated-Saturated Flow and Transport (NUFT) code (Nitao, 1995). NUFT uses the integrated-finite-difference method and simulates the transport of air, water, energy, and other species such as radionuclides. NUFT determines the spatial and temporal distribution of gas- and liquid-phase pressure, gas- and liquid-phase saturation, air-mass fraction in gas and liquid phases, water-mass fraction in gas and liquid phases, and temperature. NUFT can treat the mechanical dispersion of components. NUFT was successfully benchmarked against the VTOUGH code (Nitao, 1988), which has been qualified for quality-affecting work, and was recently qualified for quality-affecting work, according to the individual software plan for NUFT.

The following description pertains primarily to the USNT module of NUFT, which is used for solving the nonisothermal flow and transport equations of a multiphase system with multiple components. The NUFT code can solve 1-D, 2-D, and 3-D problems. The dual-permeability method options are used to represent fracture–matrix interaction. In general, any number of components and fluid phases is possible. For Yucca Mountain (YM) repository-related TH simulations, two components are generally assumed: air (a) and water (w); two phases are also assumed: gas (gas) and liquid (liq).

Vapor-pressure lowering is always applied for YM repository simulations. The solid phase is assumed to be nondeformable, although NUFT has the ability to handle isotropic solid compressibility in response to fluid pressure. Heat transfer by thermal radiation is also included in the code.

The preprocessing code YMESH generates the grid input files for NUFT drift-scale, mountain-scale, and multiscale models. YMESH utilizes user-specified criteria to vertically size the grid blocks for these models, in accordance with hydrostratigraphy information from the unsaturated-zone (UZ) site-scale model (Bodvarsson et al., 1997). The vertical extent of each hydrostratigraphic unit is honored, and the areal geometry of the UZ site-scale model is honored in 3-D models. The drift-scale models typically contain 80 or 81 grid blocks in the

vertical direction. YMESH is one of a family of pre- and postprocessors associated with NUFT. The preprocessor code RADPRO (radiation processor) is used to prepare the radiation connectivity information for NUFT models that simulate in-drift conditions.

2.1.2 Dual-Permeability Method

Three principal classes of the mathematical treatment of fracture–matrix interaction are used in the TH models. These classes are the equivalent-continuum method (ECM), the dual-permeability method (DKM), and discrete-fracture method (DFM). The DKM was used in this study.

The DKM treats the matrix and the fractures as two distinct porous continua, with transfer terms to represent the mass and heat flux between them. Because the DKM does not assume capillary-pressure equilibrium between fracture and matrix continua, it can handle much larger liquid-phase fluxes than the ECM without producing conditions near 100% liquid saturation in the matrix. The DKM also allows thermodynamic disequilibrium between matrix blocks and the adjoining fractures because of its capability to represent heat flow between these two continua.

The DKM approach has been applied in drift-scale TH models supporting Total System Performance Assessment–Viability Assessment (TSPA-VA), with direct bearing on prediction of conditions in the near field and altered zone (NF/AZ). The DKM is applied to all the line-averaged-heat-source, drift-scale, thermohydrologic (LDTH) model calculations used in the multiscale TH modeling approach to predict NFE conditions for performance assessment. In this family of models, the fracture-to-matrix liquid flow is strongly influenced by the FMX factor, which is specified for each hydrostratigraphic unit as a model input. This parameter varies between 0 and 1, and quantifies the fraction of the fracture surfaces that are wetted by the liquid phase. This fraction, together with a specified value for the fracture spacing, quantifies the interfacial flow area per unit volume of the rock matrix available for fracture-to-matrix liquid transfer.

The FMX parameter for liquid-phase interaction accounts for channeling of flow as the liquid phase "fingers" through the fracture network. However, this factor probably underrepresents the wetted surface area of fractures that occurs during condensate drainage in TH models. Other approaches (Ho, 1997) attempt to account dynamically for changes in the influence of condensate drainage on the fracture–matrix interaction. In such approaches, the parameter that is analogous to FMX increases with the magnitude of liquid flux in the fracture continuum. Because repository decay heat will generally produce greater liquid flux than that which occurs at ambient conditions, and because condensate flow may be more ubiquitous than ambient percolation in fractures, this dynamic approach results in a larger value of the interaction factor where condensate flow develops. As the repository heat output declines, thermally driven reflux decreases asymptotically toward the ambient percolation, and the interaction factor decreases to its previous value. The drift-scale TH calculations supporting TSPA-VA, and which were used in this study, assume a constant value for FMX rather than using the dynamic-FMX approach. All DKM models supporting TSPA–VA applied the same constant-FMX approach to approximating fracture-matrix interaction (CRWMS M&O, 1998).

2.1.3 Hydrostratigraphy and Infiltration-Flux Distribution

The relationship between the hydrogeologic model units represented in the models and the geological formations is shown in **Table 2-1**. The model-layer names are taken from the 3-D UZ flow model (Bodvarsson et al., 1997).

Table 2-1 Relations among model hydrogeologic units and geologic formations, geologic framework model (DTN LB970601233129.001)

Geologic unit	Welding intensity [a] / formation name (Buesch et al., 1995)	Model layer	Hydrogeologic unit
Paintbrush Group			
Tiva Canyon Tuff	M,D (Tpcpll) M,D (Tpcpln)	tcw11 tcw12	**Tiva Canyon Tuff**
	D-Basal vitrophyre (Tpcpv3) M (Tpcpv2)	tcw13	
	N,P (Tpcpv1)		**Paintbrush (PTn)**
Bedded tuff	N (Tpbt4)	ptn21	
Yucca Mountain Tuff	N,P,M (Tpy)	ptn22	
Bedded tuff	N (Tpbt3)	ptn23	
Pah Canyon Tuff	N,P,M (Tpp)	ptn24	
	N (Tpbt2)	ptn25	
Bedded tuff	N,P (Tptrv3)		
Topopah Spring Tuff	M (Tptrv2) D-Upper vitrophyre (Tptrv1)	tsw31	**Topopah Spring (TSw)**
	M,D (Tptrn)	tsw32	
	M,D,L (Tptrl); M,D,L (Tptpul)	tsw33	
	D (Tptpmn)	tsw34	
	M,D,L (Tptpll)	tsw35	
	D (Tptpln)	tsw36	
	D-Basal vitrophyre (Tptpv3)	tsw37	
	N,P,M; may be altered (Tptpv1, Tptpv2)	ch1(vc or zc)	**Calico Hills (CHn)**
Bedded tuff	N; may be altered (Tpbt1)		
Calico Hills Formation	N; unaltered (Tac-vitric)	ch2(vc or zc)	
	N; altered (Tac-zeolitic)	ch3(vc or zc)	
Bedded tuff	N; may be altered (Thtbt)	ch4(vc or zc)	
Crater Flat Group			
Prow Pass Tuff	N; may be altered (Tcp) Unit 4		
	P,M Unit 3	pp3vp	
	N,P; generally altered Units 2,1	pp2zp	
Bedded tuff	N; generally altered (Tcpbt)		
Crater Flat Group			
Upper Bullfrog Tuff	N,P; generally altered (Tcb)		
Middle Bullfrog Tuff	P,M	bf3vp	

Geologic unit	Welding intensity [a] / formation name (Buesch et al., 1995)	Model layer	Hydrogeologic unit
Lower Bullfrog Tuff	N,P; generally altered		**Crater Flat**
Bedded tuff	N; generally altered (Tcbbt)	bf2zp	**Undifferentiated (CFu)**
Upper Tram Tuff	N,P; generally altered (Tct)		
Older tuffs and lavas	Generally altered (Tct)	tr3zp; tr2zp	

[a] D = Densely; L = Lithophysal Zone; M = Moderately; N = Non; P = Partially

The following description of the site hydrostratigraphy, topography, and repository geometry is drawn from the UZ site-scale model (Bodvarsson et al., 1997). **Figure 2-1a** shows the depth of the repository horizon below the ground surface. The summit of Yucca Mountain is parallel to (and approximately one-fourth of the way from) the western edge of the repository. Because the repository is close to being horizontal (with a northward dip of about 1.6%), the repository depth contours correspond to the surface topography. The water table is approximately 350 m deeper than the repository. The ground surface slopes steeply downward to the west of the summit and less steeply to the east of the summit. The depression in the northeast corner of the repository corresponds to drill-hole wash. The repository depth plays an important role in the thermal evolution of YM after the emplacement of heat-producing high-level nuclear waste.

Figure 2-1. Surface topography, shallow infiltration, repository footprint, and model domain for site-scale thermal modeling at Yucca Mountain

(a) Depth of repository horizon below ground surface

(b) Infiltration-flux distribution over the approximate repository region

(c) Submodel locations on actual repository region

(d) Frequency histogram for infiltration flux, corresponding to the contour map of (b)

Figure 2-1b is a contour map of the infiltration-flux q_{inf} distribution over the repository region at Yucca Mountain, based on the work of Flint et al. (1996a). The boundary of the repository area shown in Figure 2-1a and Figure 2-1b is approximated as a rectangle, which was used in the TSPA-VA TH models and in this study. The actual repository area shown in **Figure 2-1c** deviates slightly from this idealized rectangle along the northern, western, and southern edges of the repository. Figure 2-1c also shows an array of 5 dots east–west by 7 dots north–south, which represents the locations of 1-D and 2-D drift-scale submodels described subsequently. These locations were chosen to sample the variability in depth to the repository from the ground surface and the spatial variation in infiltration flux.

The 35 drift-scale-model locations, including the repository depth and host-rock unit, are summarized in **Table 2-2**. Because the spatial attenuation of infiltration flux is assumed to be small above the repository horizon (CRWMS M&O, 1998), the percolation-flux distribution at the repository horizon is equivalent to the infiltration-flux distribution; therefore, Figure 2-1b is equivalent to the percolation-flux distribution assumed in this study. **Table 2-3** summarizes the percolation flux and initial liquid-phase saturation at the 35 drift-scale-model locations. The percolation flux for each location is obtained by interpolation from the infiltration-flux map (Figure 2-1b). The data for the infiltration-flux map is very dense, with

data points being spaced every 30 m in a square grid. Several different weighting schemes were tried to interpolate the percolation fluxes for each of the 35 drift-scale-model locations, ranging from a nearest-neighbor scheme to linear interpolation. To preserve some of the spatial heterogeneity in the infiltration-flux distribution, it was decided to use an exponential weighting function with a radius of influence of 50 m. Effectively, this scheme results in a percolation-flux distribution that lies somewhere between one that would arise from a nearest-neighbor scheme and one resulting from linear interpolation. The liquid-phase saturation in Table 2-3 is obtained by conducting 1-D initialization NUFT-model calculations; these calculations are conducted at each of the drift-scale-model locations with the local value of infiltration flux for that location. The 1-D initialization run is conducted until a steady-state liquid-phase saturation profile is obtained.

Table 2-2. Drift-scale model column locations

Column	Easting (m) [a]	Northing (m) [a]	Repository elev. (m)	Repository depth (m)	Unit name
l1c1	170190	232406	1093.3	387.3	Tsw36
l1c2	170417	232394	1092.5	365.3	Tsw35
l1c3	170644	232382	1091.6	335.2	Tsw35
l1c4	170871	232370	1090.8	288.1	Tsw35
l1c5	171098	232358	1089.9	274.4	Tsw34
l2c1	170214	232857	1087.0	296.2	Tsw36
l2c2	170441	232845	1086.2	369.8	Tsw35
l2c3	170668	232833	1085.4	341.5	Tsw35
l2c4	170895	232821	1084.5	278.9	Tsw35
l2c5	171122	232809	1083.7	230.6	Tsw34
l3c1	170238	233308	1080.8	329.9	Tsw36
l3c2	170464	233296	1079.9	382.6	Tsw35
l3c3	170691	233285	1079.1	298.8	Tsw35
l3c4	170918	233273	1078.2	258.5	Tsw35
l3c5	171145	233261	1077.4	256.0	Tsw34
l4c1	170261	233760	1074.5	369.8	Tsw36
l4c2	170488	233748	1073.7	386.6	Tsw35
l4c3	170715	233736	1072.8	352.6	Tsw35
l4c4	170942	233724	1072.0	293.7	Tsw35
l4c5	171169	233712	1071.1	253.7	Tsw34
l5c1	170285	234211	1068.3	400.1	Tsw35
l5c2	170512	234199	1067.4	384.3	Tsw35
l5c3	170739	234187	1066.6	357.0	Tsw35
l5c4	170966	234175	1065.7	303.2	Tsw35
l5c5	171193	234164	1064.9	281.9	Tsw34
l6c1	170309	234663	1062.0	365.0	Tsw36
l6c2	170535	234651	1061.2	396.9	Tsw35
l6c3	170762	234639	1060.3	340.2	Tsw35
l6c4	170989	234627	1059.5	295.7	Tsw35
l6c5	171216	234615	1058.6	243.0	Tsw35

Column	Easting (m) [a]	Northing (m) [a]	Repository elev. (m)	Repository depth (m)	Unit name
l7c1	170332	235114	1055.7	408.8	Tsw35
l7c2	170559	235102	1054.9	371.7	Tsw35
l7c3	170786	235090	1054.0	291.7	Tsw35
l7c4	171013	235078	1053.2	346.9	Tsw35
l7c5	171240	235066	1052.4	317.8	Tsw35

[a] Northing and easting values are given in the Nevada State Plane coordinate system.

Table 2-3. Percolation q_{perc} (mm/yr) and liquid-phase saturation $S_{liq.rep}$ at the repository depth, for the columns modeled for TSPA-VA

Note that the infiltration flux and percolation flux are assumed to be equivalent (CRWMS M&O, 1998)

Column name	q_{inf} (mm/yr)			$S_{liq.rep}$		
	0.33 x q_{inf}	1 x q_{inf}	3 x q_{inf}	0.33 x q_{inf}	1 x q_{inf}	3 x q_{inf}
l1c1	4.1	12.4	37.1	0.966	0.948	0.943
l1c2	4.5	13.4	40.3	0.896	0.885	0.888
l1c3	2.3	7.0	21.1	0.869	0.863	0.874
l1c4	1.8	5.4	16.1	0.916	0.920	0.946
l1c5	1.6	4.8	14.3	0.965	0.968	0.984
l2c1	1.1	3.3	10.0	0.940	0.937	0.937
l2c2	3.6	10.9	32.8	0.890	0.881	0.885
l2c3	5.8	17.3	51.9	0.926	0.922	0.926
l2c4	2.3	7.0	21.0	0.916	0.918	0.941
l2c5	2.8	8.5	25.6	0.964	0.967	0.986
l3c1	2.0	5.9	17.8	0.942	0.930	0.927
l3c2	5.8	17.4	52.1	0.909	0.896	0.903
l3c3	2.5	7.5	22.4	0.919	0.922	0.927
l3c4	1.6	4.8	14.3	0.915	0.920	0.946
l3c5	1.1	3.3	9.8	0.963	0.968	0.982
l4c1	2.0	6.0	18.0	0.860	0.850	0.846
l4c2	5.3	16.0	48.1	0.905	0.893	0.895
l4c3	3.6	10.9	32.7	0.925	0.925	0.936
l4c4	2.1	6.2	18.6	0.935	0.939	0.956
l4c5	1.2	3.5	10.4	0.963	0.968	0.981
l5c1	3.7	11.2	33.6	0.863	0.850	0.844
l5c2	2.8	8.5	25.6	0.924	0.926	0.935
l5c3	5.1	15.3	45.8	0.928	0.927	0.935
l5c4	0.7	2.0	6.1	0.911	0.920	0.934
l5c5	0.2	0.7	2.0	0.958	0.967	0.979
l6c1	3.1	9.4	28.1	0.883	0.865	0.859
l6c2	2.6	7.7	23.0	0.893	0.890	0.895
l6c3	4.9	14.7	44.1	0.927	0.925	0.935
l6c4	0.9	2.6	7.7	0.913	0.921	0.947
l6c5	1.2	3.7	11.0	0.933	0.938	0.955

Column name	q_{inf} (mm/yr)			$S_{liq.rep}$		
	0.33 x q_{inf}	1 x q_{inf}	3 x q_{inf}	0.33 x q_{inf}	1 x q_{inf}	3 x q_{inf}
l7c1	2.5	7.5	22.4	0.898	0.896	0.898
l7c2	1.0	2.9	8.8	0.887	0.892	0.900
l7c3	1.4	4.2	12.5	0.919	0.929	0.976
l7c4	2.0	6.0	17.9	0.918	0.921	0.940
l7c5	1.8	5.3	16.0	0.915	0.919	0.940

2.1.4 Model Geometry, Boundary Conditions, and Numerical Mesh

2.1.4.1 Drift-Scale Submodels

The 2-D drift-scale models are in the x–z plane, oriented north–south and perpendicular to the east–west emplacement-drift axis. These models are called line-averaged-heat-source, drift-scale, thermohydrologic (LDTH) models. The manner in which they are incorporated into the multiscale TH model is described in the following section. The vertical distribution for five drift-scale model locations is shown in **Figure 2-2**. In the z direction (depth), the hydrostratigraphic units correspond to those used in the site scale UZ model, with the ground surface at the top (model unit tcw11) and the water table at the bottom (model unit bf3vb). There is no lateral variation in hydrologic or thermal properties, and the x domain is treated as an infinite repetition of identical drifts with uniform interdrift spacing (this is equivalent to periodic boundaries in the x direction). By symmetry, an element from the drift centerline to the midpoint between drifts will have closed boundaries to both mass and heat flow. This basic symmetry element makes up the model domain. Mountain-scale lateral heat and mass flow are neglected. The error introduced is believed to be small for locations near the center of the repository, but it is probably significant for the edges of the repository. However, the influence of mountain-scale heat flow (and edge-cooling effects) are accounted for in the multiscale TH modeling approach described in Section 2.1.4.2.

Figure 2-2. Vertical distribution of hydrostratigraphic model units shown for drift-scale model locations (in Nevada-State coordinates) (columns l4c1–l4c5)

The current reference point-load design with no backfill was analyzed for this study. The point-load design has a drift spacing of 28 m and a lineal mass loading (LML) of 0.588 MTU/m.

The water table is a constant-property boundary with specified fixed temperature T, liquid saturation S_{liq}, and gas pressure P_{gas}. The ground surface is a constant-property boundary with specified fixed T, P_{gas}, and RH. The RH at the ground surface is assumed to be 100%; this assumption virtually eliminates vapor flux and is consistent with fixing the infiltration flux at this boundary.

The values of T at the water table and ground-surface boundaries are taken from the site-scale UZ flow model (Bodvarsson et al., 1997). At the water table, $S_{liq} = 100\%$. The value of P_{gas} at the ground surface is taken from the site-scale UZ flow model. The value of P_{gas} at the water table is consistent with the value of P_{gas} at the ground surface and the pressure profile of a static gas column from the ground surface to the water table.

Figure 2-3 is a vertical cross-section of the emplacement drift, orthogonal to the drift axis in the 2-D LDTH and 3-D discrete-heat source, drift-scale, thermal conduction-only (DDT) models. By using periodic boundaries, the centerline of the drift becomes an axis of symmetry and, consequently, provides an adiabatic, no-flow boundary. The centerline of the pillar between drifts provides the other adiabatic, no-flow boundary in the x direction.

Figure 2-3. Vertical cross-section of the emplacement drift in the DDT and LDTH models, showing the thermal-radiation connections among the surfaces in the drift that are used in thermal simulations

For the current design, the waste-package (WP) diameter is 1.67 m, and the emplacement-drift diameter is 5.1 m. The invert, which is at the bottom of the drift, is assumed to occupy 16.6% of the drift cross-section. As demonstrated previously (Buscheck, 1996), a circular WP in a circular drift can be accurately represented by a square WP in a square drift, provided that the respective circular and square cross-sectional areas are equal. In the model, the WP dimensions are 1.445 m × 1.445 m, and the drift measures 4.52 m × 4.52 m. The invert, which occupies the lower 16.6% of the drift, is assumed to be filled with concrete, consisting of fractured and jointed matrix blocks. The same cross-sectional geometry is used for the LDTH and DDT models.

Heat flux from the WP sources is averaged over the length of the drifts and coupled to the drift surfaces primarily by radiant heat transfer. Thermal radiation is also accounted for between different locations on the drift surface. An efficient heat-transfer mechanism distributes the heat flux uniformly to the perimeter surfaces of the emplacement drift. The drift-wall and drift-floor surfaces are assumed to be blackbodies ($\varepsilon = 1$), and the WPs have $\varepsilon = 0.8$. This allows the use of a constant heat-flux boundary condition at the drift perimeter.

The value of P_{gas} at the water table is established when the models are initialized at ambient conditions. The initialization model runs are continued until the distributions of T, S_{liq}, P_{gas}, and gas-phase air-mass fraction $X_{air,gas}$ in the model attain steady-state distributions.

The DKM approximation is used to represent fracture–matrix coupling. Because different properties are assigned to fracture elements and matrix elements, two grid blocks have to be assigned to each spatial location (i.e., twice as many as would be required to give the same spatial resolution with the ECM).

The 2-D (LDTH) and 3-D (DDT) drift-scale models utilize geometric symmetry; therefore, these models extend from the centerline of the WPs to the centerline of the pillar that separates the drifts. In the 2-D LDTH model, 16 grid blocks are used in the x direction for the point-load design. In the vertical direction, 80 grid-block layers are used to represent the hydrostratigraphy; thus, the point-load design requires 1240 grid blocks.

The 3-D DDT model represents the full 3-D geometry of the emplacement drifts, including the invert; WPs; the open drift lying below, above, and to the side of the WPs; and the open drift lying axially between WPs (**Figure 2-4**).

Figure 2-4. Plan view of the WP layout represented in the DDT model

The 1-D drift-scale model — namely, the smeared-heat-source, drift-scale thermal-conduction (SDT) model — has the same vertical grid-block spacing as the 2-D and 3-D drift-scale models. The vertical distribution of thermal properties is the same in the SDT, LDTH, and DDT models.

2.1.4.2 Mountain-Scale Submodels

The 3-D smeared-heat-source, mountain-scale thermal-conduction (SMT) submodel enables the multiscale TH modeling approach to capture the influence of surface topography and edge-cooling effects on repository temperature. Temperature predictions are then used for interpolating other performance measures. The SMT model also captures the influence of the thermal-property distribution in the mountain on the overall temperature distribution. The specific SMT model input to the multiscale TH modeling approach is the repository host-rock temperature T_{rep} (SMT). Because the SMT results are predicted with a thermal-conduction model, it is likely that temperatures above the boiling point will be overpredicted relative to those predicted by a TH model.

Transient, 3-D, conduction-only problems can be solved readily by NUFT, permitting the use of fine lateral and vertical grid-block spacing in the repository area. At the repository edges, a lateral grid-block spacing of 15 m is used. In the vertical interval that corresponds to the dryout zone in TH models, a vertical grid-block spacing of about 4 m is used.

The repository is represented as a rectangular approximation of the actual shape (Figure 2-1b). The long axis of the repository is oriented three degrees from the north. The SMT model assumes the north–south length of the repository to be 2912 m (the product of 104 emplacement drifts times the drift spacing of 28 m). The SMT model assumes the east–west width of the repository to be 1109 m (the area of the overall heated repository footprint — 3.23 km^2 or 798 acres — divided by 2912 m).

The SMT model encompasses the entire unsaturated zone (UZ) and the upper 1000 m of the saturated zone (SZ). Topography, stratigraphy, thermal properties, temperature boundary conditions, and initial temperature are consistent with the UZ site-scale model (Bodvarsson and Bandurraga, 1996; Bodvarsson et al., 1997). Because the SMT model extends below the lower boundary of the UZ site-scale model, it is necessary to vertically extrapolate the temperature distribution from the UZ site-scale model below the water table. The influence of dryout on rock thermal conductivity K_{th} is approximated with the use of a K_{th} vs. temperature T relation. The dependence of K_{th} on liquid-phase saturation S_{liq} is approximated by correlating T computed with a 1-D SDT model, with S_{liq} in a corresponding 1-D smeared-heat-source, drift-scale thermohydrologic (SDTH) model, and developing a functional relation between K_{th} and T predicted by the SDT model. The K_{th} vs. T relation in the SDT model mimics the K_{th} vs. S_{liq} in the SDTH model.

For an areal mass loading (AML) of 85 MTU/acre (calculated on the basis of commercial spent nuclear fuel [CSNF]) and 63,000 MTU of CSNF, the repository area is calculated to be only 741 acres, which is 7.5% less than the 798-acre repository area assumed in the SMT model. However, 4 of the 104 emplacement drifts are left empty, thus about 4% of the repository drifts are not directly heated by WPs. The bulkheads that will separate the emplacement drifts from the perimeter drifts are located about 30 m from the outermost WPs at the eastern and western ends of the emplacement drifts. Heat-transfer mechanisms, such as the cold-trap effect (Buscheck, 1996; Buscheck et al., 1996) and thermal radiation will efficiently distribute the decay heat well beyond the outermost WPs. The assumption is effectively made that decay heat is axially spread 18 m beyond the outermost WPs at either end of the drifts, thereby increasing the effective heated length of the emplacement drift by 36 m. When these adjustments are made, the heated footprint of the repository becomes 798 acres, and the effective AML becomes 78.9 MTU/acre. Thermal-loading by the reference

85-MTU/acre repository is represented as a uniform, 4.52-m-thick, smeared heat source over a 798-acre heated footprint, based on a composite of the decay curves for the entire waste inventory (see Table 2-4 in Section 2.1.5).

The SMT model represents the 1.6% south-to-north dip of the repository. In the east–west direction, the repository is represented as being horizontal. For the actual repository, the eastern and western boundaries have the same elevation, whereas the center of the repository (in the east–west direction) is elevated by about 3 m relative to the eastern and western edges. This small rise at the center of the repository is neglected in the SMT model.

The numerical grid for the SMT consists of three concentric nests of grid blocks. The preprocessor YMESH determines the areal dimensions of the grid blocks on the basis of user-specified dimensions for each of the nests. YMESH determines the vertical grid-block spacing on the basis of user-specified criteria and honoring the unit contacts in the UZ site-scale model. The vertical spacing criteria are specified for each nest. The objective is to provide fine spatial resolution in the repository area, with the grid refinement increasing in proximity to the repository edges. Because of the large number of model units, relatively fine vertical grid refinement occurs over the entire UZ, particularly within the Paintbrush Tuff (ptn21–ptn25) units.

2.1.5 Thermal-Loading Conditions Assumed in the Models

The TSPA-VA TH predictions are for the reference AML of 85 MTU/acre, which is based on the total MTU of emplaced CSNF and which neglects the MTU of other waste forms such as defense high-level waste (DHLW). The inventory of WPs that is assumed to be emplaced at Yucca Mountain consists of several major WP types, including the following:

- **CSNF WPs**, roughly half of which contains pressurized-water-reactor (PWR) fuel assemblies and the other half boiling-water-reactor (BWR) fuel assemblies: The heat output from CSNF WPs varies widely from design-basis fuel WPs that have a high heat output to older WPs that have a relatively low heat output.
- **Co-disposal DHLW WPs** that contain DHLW glass logs and spent nuclear fuel (SNF): Co-disposal DHLW WPs produce relatively little heat.
- **Direct-disposal DOE SNF WPs** that contain Department of Energy (DOE) SNF: These WPs produce relatively little heat.

For mountain-scale model calculations, it is assumed that the repository-wide thermal-loading conditions can be characterized by a uniform radioactive heat-of-decay curve (**Table 2-4)**, which is a blend of the heat-of-decay curves from the entire inventory of WPs emplaced in the repository (Bahney, 1997). This curve is based on the total number of assemblies of the two major CSNF types (BWR and PWR), the total heat output from DHLW, and the major heat component of the DOE SNF. The repository-wide heat output assumes 63,000 MTU of CSNF, 4667 MTU of DHLW, and 2333 MTU of the DOE SNF waste. For an 85-MTU/acre repository, this results in a repository area of 741 acres. The actual repository area is slightly larger (798 acres) because about 7.5% of the repository area does not contain WPs.

Table 2-4. Summary of the WP heat sources used in submodels for the multiscale approach

LDTH, SDT, and DDT submodels					
WP type	WPs in model	MTU per WP	WP heat output (kW)		
			0 yr	100 yr	1000 yr
12-PWR high-heat CSNF	7.14%	5.436	10.477	2.556	0.464
21-PWR low-heat CSNF	14.29%	8.148	2.905	0.823	0.223
21-PWR design-basis CSNF	14.29%	9.744	17.85	4.408	0.789
21-PWR medium-heat CSNF	14.29%	9.051	9.338	2.580	0.551
44-BWR CSNF	28.57%	7.876	6.440	1.917	0.422
Co-disposal DHLW	14.29%	N/A	4.058	0.351	0.130
Direct-disposal DOE DHLW	7.14%	N/A	0.793	0.292	0.123

Mountain-scale SMT model				
AML (MTU/acre)	Areal power density (kW/acre)			
	0 yr	100 yr	1000 yr	10,000 yr
78.9	92.317	23.606	4.838	1.217

N/A = "not available"

For drift-scale model calculations, it is assumed that the thermal-decay curves for seven WP types in Figure 2-4 and Table 2-4 are representative of the wide range of WPs to be emplaced in the repository. These seven WP types span the range of heat output, from the high-output CSNF WPs to the low-output DHLW WPs.

The SDT, LDTH, and DDT models all assume the same seven WP types pictured in Figure 2-4 and the WP percentages listed in Table 2-4. The eight WPs represented in the DDT model consist of these seven WP types and one extra 44-BWR CSNF WP or, stated alternatively, six full WPs and two half WPs (the 12-PWR CSNF WP and the direct-disposal DOE DHLW WP). The LDTH model uses a heat-source decay curve that is an average of the decay curves for the eight individual WPs represented in the DDT model. In other words, the LDTH model smears the heat output from a conduction-only model, which uses discrete heat sources, into a line-averaged heat source.

2.2 Multiscale Thermohydrologic Modeling Methodology

The multiscale TH model approach is used to develop time-varying estimates of key EBS and NFE performance measures for locations throughout the repository. The predicted EBS/NFE performance measures can vary significantly for different locations because of differences in hydrostratigraphy and infiltration flux. The performance measures include drift-wall temperature, WP temperature, and drift-air *RH* at the WP surface (see **Table 2-5**). The estimation procedure is fast enough to be conducted for a dense grid of uniformly spaced locations in the repository layout and repeated for TSPA-VA sensitivity cases and alternative model exercises.

Table 2-5. Thermohydrologic measures estimated by the multiscale TH modeling approach

✓ = Measures calculated for TSPA-VA
✖ = Other measures also calculated by the approach

Location	Temperature	Relative humidity	Gas-phase air-mass fraction ($X_{air,gas}$)	Liquid-phase saturation	Liquid-phase flux
Rock above drift wall	✖	✖	✖	✖	✓
Rock at drift wall	✓	✓	✖	✖	✖
Drift above WP			✓		
WP surface	✓	✓			✖
Invert	✖	✖	✖	✓	✖

The need for a multiscale modeling approach stems from the fact that the performance measures depend on TH behavior within a few meters of the emplacement drifts and on thermal and TH behavior on a repository (or mountain) scale. A single numerical model cannot readily incorporate the required range of scales, for locations throughout the repository, without involving an unfeasible number of grid blocks. Consequently, a procedure has been developed for estimating the results that would be obtained using a full-scale, 3-D repository model with drift-scale resolution (i.e., millions of grid blocks).

A possible (brute-force) approach to the multiscale prediction problem would be to embed a 3-D drift-scale model with a relatively fine mesh into a 3-D repository-scale model with a coarse mesh. This approach is also too computationally intensive for the required number of cases. The multiscale approach presented subsequently combines 1-D, 2-D, and 3-D thermal-conduction-only models (T-models) and TH models at different scales to estimate the required performance measures (see Section 2.2.1.1).

The multiscale TH model approach captures the key factors influencing TH conditions in the EBS and NFE. The three most important factors are:

- Mountain-scale (or repository-scale) heat flow, including the influence of lateral heat loss at the edge of the repository
- Repository-scale variability in percolation flux
- WP-to-WP variability in heat output

The approach also accounts for additional important factors influencing TH conditions in the EBS and NFE, including:

- Matrix imbibition diffusivity of the local host-rock unit (which governs the rate of capillary-driven rewetting in the rock matrix)
- Wet and dry thermal conductivity of the local host-rock unit
- Repository depth (overburden thickness)

2.2.1 Multiscale Submodels

The multiscale approach combines 1-D, 2-D, and 3-D drift-scale thermal-conduction and TH models with a conduction-only 3-D mountain-scale model (Figure 2-5). Output from this system provides estimates for the time evolution of the performance measures summarized in Table 2-6. These measures are used by TSPA-VA to estimate WP corrosion rates, waste-form dissolution rates, and transport of radionuclides in the NFE.

Figure 2-5. Schematic of conceptual models used by the multiscale TH modeling approach

Table 2-6, Summary of model types used in the multiscale TH modeling approach

Model type	Heat source	Dimensionality	Process type [a]	In-drift thermal radiation	Use in TSPA-VA multiscale TH modeling approach
SMT	smeared	3-D mountain-scale	T	no	Process-model input
SMTH	smeared	3-D mountain-scale	TH	no	Process-model input [b]
LMTH	line-averaged	3-D mountain-scale	TH	yes	Abstracted result [c]
DMTH	discrete	3-D mountain-scale	TH	yes	Abstracted result [c]
SDT	smeared	1-D drift-scale	T	no	Process-model input
SDTH	smeared	1-D drift-scale	TH	no	Process-model input [b]
LDTH	line-averaged	2-D drift-scale	TH	yes	Process-model input
DDT	discrete	3-D drift-scale	T	yes	Process-model input
DDTH	discrete	3-D drift-scale	TH	yes	Model-abstraction testing

[a] T = thermal-conduction; TH = thermohydrologic
[b] to be used in a future version of the multiscale TH modeling approach
[c] See Figure 2-5.

Four different submodel types are used by the multiscale TH modeling approach (Table 2-6):

- **S**meared-heat source, **m**ountain-scale **t**hermal conduction-only (SMT) model
- **S**meared-heat source, **d**rift-scale, **t**hermal conduction-only (SDT) model
- **L**ine-averaged heat source, **d**rift-scale, **TH** (LDTH) models that use the DKM conceptual model
- **D**iscrete-heat source, **d**rift-scale, **t**hermal conduction-only (DDT) models

Other submodel types are approximated by combining or modifying the four basic types. These derivative submodels include:

- **L**ine-averaged-heat-source, **m**ountain-scale **TH** (LMTH) models
- **D**iscrete-heat source, **m**ountain-scale **TH** (DMTH) models
- **D**iscrete-heat-source, **d**rift-scale **TH** (DDTH) models

The interaction of all submodel types is depicted in **Figure 2-6**.

Figure 2-6. Flow chart for the multiscale TH modeling approach for (a) cases with no engineered backfill and (b) cases with engineered backfill (Hardin et al., 1998)

2.2.1.1 Submodel Performance Measures

The TH performance measures in Table 2-6 are provided to TSPA-VA for various combinations of the following:

- Different locations in the repository
- Variations in heat production corresponding to different WP designs and types of waste (such as CSNF vs. DHLW), CSNF age and burnup, WP spacing, and sequencing of WP types in the emplacement drifts
- Design options such as the line-load design or backfill

The TH performance measures are also provided for testing sensitivity of the TSPA-VA to variations such as the following:

- Alternative thermal and hydrologic properties
- Alternative distributions of infiltration flux, including the influence of climate change
- Alternative designs, such as the point-load design and the line-load design
- Alternative EBS features, such as crushed-tuff and quartz-sand backfill

2.2.1.2 Submodel Calculations

For each of the 35 repository locations (see Table 2-2 and Table 2-3), parallel SDT and LDTH calculations are conducted for AMLs of 85, 56.67, and 42.5 MTU/acre (the lower two values represent cooler areas in the repository). This results in six model calculations per location. In addition, one DDT submodel calculation is required by the multiscale approach; additional DDT calculations may be included to capture effects from the wide range of possible WP-type and emplacement-sequence scenarios.

This procedure captures the significant effects from mountain-scale heat flow as well as drift-scale TH behavior driven by heat output from individual WPs, each having distinctively different heat-generation characteristics. To explicitly account for these effects in a single numerical TH model would require approximately 60 million grid blocks, which is beyond the computational capabilities of the current generation of TH simulators.

Altogether, using the 5×7 grid, a single TSPA-VA TH scenario requires 424 NUFT runs, including 211 2-D drift-scale calculations and one mountain-scale calculation. In a procedure that conditions the comparison of thermal conduction and TH model calculations, an additional 212 runs are used to initialize the models. Using the NUFT code, which is optimized for efficiency, a complete set of 424 runs requires 12–16 hr on 9 Sun Ultra2 Sparc workstation processors.

2.2.2 Calculational Procedure for the Multiscale TH Model

The multiscale TH modeling methodology involves seven major calculational steps (Figure 2-6). These steps are described in detail in a previous report (Hardin et al., 1998) and in the TSPA-VA Technical Basis Document (CRWMS M&O, 1998). The steps are as follows:

1. Conduct numerical simulations using NUFT code (shown as blue boxes in Figure 2-5).
2. Construct the functional relations, called scanning curves, among the various model-output variables from complementary drift-scale models (shown as yellow boxes in Figure 2-5).
3. Interpolate the distribution of average drift-wall temperature. The drift-wall temperature corresponding to a 3-D mountain-scale TH model (with emplacement drifts modeled by line-averaged heat sources) is approximated by interpolating

scanning curves. The interpolant T_{dw}(LMTH; x,y) is calculated for average drift-wall conditions using the smeared repository heat-source temperature T_{rep}(SMT; x,y) and the T_{dw}(LDTH) vs. T_{rep}(SDT) scanning curve, at the 35 locations and 3 AMLs (Figure 2-6a). This process involves spatial interpolation between the 35 locations and also involves interpolation between the 3 AML scanning curves in Figure 2-6a. The result of this step is the distribution of average drift-wall temperatures as a function of location in the repository. Because this process approximates a 3-D LMTH model prediction of the distribution of T_{dw} in the repository, the resulting distribution is called T_{dw}(LMTH; x,y), where x and y refer to the coordinate location in the repository.

4. Interpolate the distribution of drift-wall temperature for each WP type. The drift-wall temperature distribution in the repository, as a function of location, is calculated for each WP type by adding ΔT_{dw}(DDT; WP-type) to the T_{dw}(LMTH; x,y) distribution determined in step 3. The net result of this step is comparable to having a 3-D DMTH model prediction of the T_{dw} distribution in the repository for each WP type; hence, the resulting distribution is called T_{dw}(DMTH; x,y,WP-type), where x and y refer to the coordinate location in the repository.
5. Interpolate the distribution of near-field and in-drift hydrologic conditions. These distributions are interpolated for each WP type using the temperature distribution from Step 4 and the scanning curves from Step 2. The *RH* at the WP, the drift-wall matrix saturation, the liquid-phase flux above the drift, the air-mass fraction at the WP, and the invert liquid-phase saturation are calculated for each WP type, as a function of location in the repository.
6. Determine the distribution of WP temperature for each WP type. The drift-wall temperature distribution from Step 3 and scanning curves from Step 2 are used to determine the distribution of temperature on WPs throughout the repository area for each WP type. The result is the abstracted WP temperature distribution (T_{wp}) for each WP type, T_{wp}(DMTH; x,y,WP-type). This is calculated by adding the temperature variation at the WP from Step 2, ΔT_{wp}(DDT; WP-type), to the abstracted temperature for an LMTH model, T_{dw}(LMTH; x,y) obtained in Step 3. This step determines the distribution of WP temperature as a function of WP type and location in the repository. The result of this step is comparable to having a DMTH-model prediction of the T_{wp} distribution in the repository for each WP type; hence the resulting distribution is called T_{wp}(DMTH; x,y,WP-type), where x and y refer to the coordinate location in the repository.
7. Determine the distribution of relative humidity on WPs for each WP type. For cases with no backfill, *RH* on WPs is determined using the drift-wall temperature T_{dw} distribution from Step 4, the drift-wall relative humidity RH_{dw} distribution from Step 5, the WP temperature T_{wp} distribution from Step 6, and the relation $RH_{wp} = RH_{dw}[P_{sat}(T_{dw})/P_{sat}(T_{wp})]$, where P_{sat} is the saturated vapor pressure. The result of this step is the DMTH-model-predicted WP *RH* distribution, RH_{wp}(DMTH; x,y,WP-type), calculated using the abstracted drift-wall temperature T_{dw}(DMTH; x,y,WP-type), the abstracted WP temperature T_{wp}(DMTH; x,y,WP-type), and the relation $RH_{wp} = RH_{dw}[P_{sat}(T_{dw})/P_{sat}(T_{wp})]$. The result of this step is comparable to having a DMTH-model prediction of the RH_{wp} distribution in the repository for each WP type; hence the resulting distribution is called RH_{wp} (DMTH; x,y,WP-type), where x and y refer to the coordinate location in the repository. This step is carried out differently for cases with backfill, as is described in the TSPA-VA Technical Basis Document (CRWMS M&O, 1998).

2.3 Thermal and Hydrologic Properties

All NUFT-model calculations use the set of thermal properties used in all of the TSPA-VA T- and TH-model calculations, which are summarized in **Table 2-7** (Francis et al., 1997).

Table 2-7. Thermal properties for the rock matrix

Geologic unit	Model unit	K_{wet} (W/mK)	K_{dry} (W/mK)	Rock density (kg/m^3)	Specific heat (J/kgK)
Tpcp11	tcw11	1.76	1.02	2510	847
Tpcpln	tcw12	1.88	1.28	2510	837
Tpcpv	tcw13	0.98	0.54	2470	857
Tpcpv1	ptn21	0.50	0.35	2340	1080
Tpy	ptn22	0.97	0.44	2400	849
Tpbt3	ptn23	1.02	0.46	2370	1020
Tpp	ptn24	0.82	0.35	2260	1330
Tpbt2	ptn25	0.67	0.23	2370	1220
Tptrv	tsw31	1.00	0.37	2510	834
Tptrn	tsw32	1.62	1.06	2550	866
Tptpul	tsw33	1.80	0.71	2510	883
Tptpmn	tsw34	2.33	1.56	2530	948
Tptp11	tsw35	2.02	1.2	2540	900
Tptpln	tsw36	1.84	1.42	2560	865
Tptpv	tsw37	2.08	1.69	2360	984
Tpbt1	ch1zc	1.31	0.70	2310	1060
Tac(z)	ch2zc	1.20	0.61	2350	1150
Tac(z)	ch3zc	1.20	0.61	2350	1150
Tacbt	ch4zc	1.35	0.73	2440	1170
Tpbt1	ch1vc	1.31	0.70	2310	1060
Tac(v)	ch2vc	1.17	0.58	2240	1200
Tac(v)	ch3vc	1.17	0.58	2240	1200
Tabt1	ch4vc	1.17	0.58	2240	1200
Tcp(3)	pp3vp	1.26	0.66	2580	841
Tcb(w)	bf3vb	1.26	0.66	2580	841
Tcb(w)	tm3vt	1.26	0.66	2580	841
Tcp(2)	pp2zp	1.35	0.74	2510	644
Tcb(n)	bf2zb	1.35	0.74	2510	644

The following section compares the predicted TH conditions in the EBS/NFE for eight different hydrologic property sets. These eight property sets involve combinations of three unique matrix-property sets and seven unique fracture-property sets (**Table 2-8**). The matrix and fracture property values for these sets are summarized in **Table 2-9** through **Table 2-18**. In the following Tables 2-8 through 2-17, *I* stands for the nominal infiltration-flux map and α is the van Genuchten alpha parameter.

Table 2-8. Overview of hydrological-property sets used in this study

	Matrix-property set		
Fracture-property set	**7/97 *I* × 1 (also 12/97 *I* × 1, 12/97 *I* × 3, and 12/97 *I* × 0.33) (Table 2-9)**	**11/97 TH (Table 2-11)**	**12/97 modified TH (Table 2-13)**
7/97 *I* × 1 (Table 2-10)	TSPA-VA preliminary base-case *I* × 1	—	—
11/97 TH (Table 2-12)	—	11/97 TH	12/97 modified TH
12/97 *I* × 1 $\alpha_{f,mean}$ (Table 2-14)	TSPA-VA base-case *I* × 1 $\alpha_{f,mean}$	—	—
12/97 *I* × 3 $\alpha_{f,max}$ (Table 2-15)	TSPA-VA base-case *I* × 3 $\alpha_{f,max}$	—	—
12/97 *I* × 3 $\alpha_{f,min}$ (Table 2-16)	TSPA-VA base-case *I* × 3 $\alpha_{f,min}$	—	—
12/97 *I* × 0.33 $\alpha_{f,max}$ (Table 2-17)	TSPA-VA base-case *I* × 0.33 $\alpha_{f,max}$	—	—
12/97 *I* × 0.33 $\alpha_{f,min}$ (Table 2-18)	TSPA-VA base-case *I* × 0.33 $\alpha_{f,min}$	—	—

I stands for the nominal infiltration-flux map; α_f is the van Genuchten alpha parameter for fractures.

Table 2-9. Matrix property values in the TSPA-VA preliminary base-case (July 1997) *I* × 1

Also used in the TSPA-VA base case (December 1997) *I* x 1, *I* x 3, and *I* x 0.33 (CRWMS M&O, 1998)

Geologic unit	Model unit	Porosity	Permeability (m^2)	S_r [a]	α (Pa^{-1}) [b]	m [b]
Tpcp11	tcw11	0.066	5.37E–18	0.13	1.17E–06	0.232
Tpcpln	tcw12	0.066	5.37E–18	0.13	1.32E–06	0.236
Tpcpv	tcw13	0.14	4.90E–17	0.33	6.46E–07	0.427
Tpcpv1	ptn21	0.369	3.09E–14	0.10	3.80E–05	0.231
Tpy	ptn22	0.234	3.02E–15	0.14	8.71E–06	0.488
Tpbt3	ptn23	0.353	8.32E–14	0.17	4.57E–05	0.287
Tpp	ptn24	0.469	1.15E–13	0.10	4.27E–05	0.349
Tpbt2	ptn25	0.464	2.45E–13	0.10	1.95E–04	0.279
Tptrv	tsw31	0.042	4.90E–17	0.11	1.00E–05	0.237
Tptrn	tsw32	0.146	2.75E–16	0.04	2.29E–05	0.273
Tptpul	tsw33	0.135	1.15E–17	0.06	6.76E–06	0.247
Tptpmn	tsw34	0.089	4.07E–18	0.18	1.02E–06	0.322
Tptp11	tsw35	0.115	1.55E–17	0.08	3.31E–06	0.229
Tptpln	tsw36	0.092	8.91E–17	0.18	7.41E–07	0.414
Tptpv	tsw37	0.02	1.29E–17	0.50	1.55E–06	0.387

Geologic unit	Model unit	Porosity	Permeability (m^2)	S_r [a]	α (Pa^{-1}) [b]	m [b]
Tpbt1	ch1zc	0.193	1.38E–17	0.36	8.32E–07	0.366
Tac(z)	ch2zc	0.24	9.12E–18	0.20	1.95E–06	0.220
Tac(z)	ch3zc	0.24	9.12E–18	0.20	1.95E–06	0.220
Tacbt	ch4zc	0.169	1.55E–17	0.33	7.76E–07	0.477
Tpbt1	ch1vc	0.265	1.32E–12	0.04	6.61E–05	0.190
Tac(v)	ch2vc	0.321	2.57E–13	0.06	7.41E–05	0.224
Tac(v)	ch3vc	0.321	2.57E–13	0.06	7.41E–05	0.224
Tabt1	ch4vc	0.321	2.57E–13	0.06	7.41E–05	0.224
Tcp(3)	pp3vp	0.274	2.82E–15	0.07	1.74E–05	0.311
Tcb(w)	bf3vb	0.274	2.82E–15	0.07	1.74E–05	0.311
Tcb(w)	tm3vt	0.274	2.82E–15	0.07	1.74E–05	0.311
Tcp(2)	pp2zp	0.197	5.75E–17	0.18	1.66E–06	0.316
Tcb(n)	bf2zb	0.197	5.75E–17	0.18	1.66E–06	0.316

[a] S_r is the residual liquid-phase saturation (not in situ saturation).

[b] α and m are fitting parameters for capillary pressure and relative permeability curves, respectively.

Table 2-10. Fracture property values in the TSPA-VA preliminary base-case (July 1997) hydrologic parameter set for $I \times 1$ (CRWMS M&O, 1998)

Geologic unit	Model unit	Porosity	Permeability (m^2)		S_r [a]	α (Pa^{-1}) [b]	m [b]	FMX
			Vertical	Horizontal				
Tpcp11	tcw11	2.33E–04	2.29E–11	6.03E–12	0.01	2.95E–04	0.492	4.90E–04
Tpcpln	tcw12	2.99E–04	1.38E–11	6.03E–12	0.01	2.95E–04	0.492	4.90E–04
Tpcpv	tcw13	7.05E–05	2.82E–12	2.40E–13	0.01	9.12E–05	0.492	4.90E–04
Tpcpv1	ptn21	4.84E–05	5.25E–13	5.25E–13	0.01	1.10E–03	0.492	1.10E–01
Tpy	ptn22	4.83E–05	1.95E–13	1.95E–13	0.01	1.82E–03	0.492	7.08E–01
Tpbt3	ptn23	1.30E–04	2.57E–13	2.57E–13	0.01	3.39E–03	0.492	6.92E–01
Tpp	ptn24	6.94E–05	6.17E–14	6.17E–14	0.01	9.33E–04	0.492	4.79E–01
Tpbt2	ptn25	3.86E–05	7.76E–14	7.76E–14	0.10	1.95E–04	0.279	4.79E–01
Tptrv	tsw31	8.92E–05	1.07E–11	1.00E–12	0.01	3.98E–05	0.481	5.01E–01
Tptrn	tsw32	1.29E–04	1.51E–11	7.08E–13	0.01	9.33E–05	0.488	2.88E–05
Tptpul	tsw33	1.05E–04	2.63E–11	8.91E–13	0.01	1.78E–04	0.492	7.94E–05
Tptpmn	tsw34	1.24E–04	6.76E–12	4.27E–13	0.01	9.77E–05	0.492	1.55E–04
Tptp11	tsw35	3.29E–04	3.80E–12	9.12E–13	0.01	1.10E–04	0.492	7.76E–02
Tptpln	tsw36	3.99E–04	1.20E–12	1.20E–12	0.01	1.32E–04	0.492	4.79E–05
Tptpv	tsw37	4.92E–04	1.20E–12	1.20E–12	0.01	1.17E–04	0.492	4.90E–04
Tpbt1	ch1zc	1.10E–05	2.40E–14	2.40E–14	0.01	1.12E–03	0.492	1.82E–01
Tac(z)	ch2zc	1.10E–05	1.17E–14	1.17E–14	0.01	1.23E–03	0.492	1.00E+00
Tac(z)	ch3zc	1.10E–05	1.17E–14	1.17E–14	0.01	1.23E–03	0.492	1.00E+00
Tacbt	ch4zc	1.10E–05	1.55E–14	1.55E–14	0.01	1.15E–03	0.492	1.00E+00
Tpbt1	ch1vc	7.14E–05	1.74E–13	1.74E–13	0.01	1.17E–03	0.492	4.90E–01
Tac(v)	ch2vc	7.14E–05	2.88E–13	2.88E–13	0.01	1.17E–03	0.492	4.89E–01

Geologic unit	Model unit	Porosity	Permeability (m^2)		S_r [a]	α (Pa^{-1}) [b]	m [b]	FMX
			Vertical	Horizontal				
Tac(v)	ch3vc	7.14E–05	2.88E–13	2.88E–13	0.01	1.17E–03	0.492	4.89E–01
Tabt1	ch4vc	7.14E–05	2.88E–13	2.88E–13	0.01	1.17E–03	0.492	4.89E–01
Tcp(3)	pp3vp	7.14E–05	6.92E–13	6.92E–13	0.01	1.41E–03	0.492	5.13E–04
Tcb(w)	bf3vb	7.14E–05	6.92E–13	6.92E–13	0.01	1.41E–03	0.492	5.13E–04
Tcb(w)	tm3vt	7.14E–05	6.92E–13	6.92E–13	0.01	1.41E–03	0.492	5.13E–04
Tcp(2)	pp2zp	1.10E–05	6.46E–14	6.46E–14	0.01	3.72E–04	0.492	4.89E–01
Tcb(n)	bf2zb	1.10E–05	6.46E–14	6.46E–14	0.01	3.72E–04	0.492	4.89E–01

[a] S_r is the residual liquid-phase saturation (not in situ saturation).

[b] α and m are fitting parameters for capillary pressure and relative permeability curves, respectively.

Table 2-11. Matrix property values for the November 1997 TH hydrologic parameter set calibrated against the Single-Heater Test (SHT) (Hardin et al., 1998)

Geologic unit	Model unit	Porosity	Permeability (m^2)	S_r [a]	α (Pa^{-1}) [b]	m [b]
Tpcp11	tcw11	0.066	5.40E–18	0.13	1.15E–06	0.2310
Tpcpln	tcw12	0.066	5.40E–18	0.13	2.01E–06	0.2447
Tpcpv	tcw13	0.140	5.69E–17	0.33	3.74E–06	0.4548
Tpcpv1	ptn21	0.369	1.61E–14	0.10	3.98E–05	0.2531
Tpy	ptn22	0.234	3.30E–15	0.14	7.94E–06	0.4925
Tpbt3	ptn23	0.353	5.40E–14	0.17	5.44E–05	0.3002
Tpp	ptn24	0.469	8.80E–14	0.10	3.43E–05	0.3859
Tpbt2	ptn25	0.464	3.18E–13	0.10	1.81E–04	0.3195
Tptrv	tsw31	0.042	7.76E–17	0.11	5.84E–05	0.2304
Tptrn	tsw32	0.146	1.82E–16	0.04	2.00E–05	0.2861
Tptpul	tsw33	0.135	2.04E–17	0.06	6.21E–06	0.2479
Tptpmn	tsw34	0.089	4.08E–18	0.18	1.19E–06	0.3212
Tptp11	tsw35	0.115	2.22E–17	0.08	4.01E–06	0.1983
Tptpln	tsw36	0.092	8.70E–18	0.18	8.08E–07	0.5138
Tptpv	tsw37	0.020	8.39E–18	0.50	5.30E–07	0.3709
Tpbt1	ch1zc	0.193	1.36E–17	0.36	4.29E–06	0.3489
Tac(z)	ch2zc	0.240	2.50E–18	0.20	2.16E–05	0.2119
Tac(z)	ch3zc	0.240	2.50E–18	0.20	2.16E–05	0.2119
Tacbt	ch4zc	0.169	5.49E–18	0.33	1.03E–06	0.4322
Tpbt1	ch1vc	0.265	1.60E–12	0.04	7.60E–05	0.1592
Tac(v)	ch2vc	0.321	5.50E–14	0.06	4.12E–05	0.2291
Tac(v)	ch3vc	0.321	5.50E–14	0.06	4.12E–05	0.2291
Tabt1	ch4vc	0.321	5.50E–14	0.06	4.12E–05	0.2291
Tcp(3)	pp3vp	0.274	1.91E–15	0.07	1.66E–05	0.3142

Geologic unit	Model unit	Porosity	Permeability (m^2)	S_r [a]	α (Pa^{-1}) [b]	m [b]
Tcb(w)	bf3vb	0.274	1.91E–15	0.07	1.66E–05	0.3142
Tcb(w)	tm3vt	0.274	1.91E–15	0.07	1.66E–05	0.3142
Tcp(2)	pp2zp	0.197	1.75E–17	0.18	8.39E–06	0.3568
Tcb(n)	bf2zb	0.197	1.75E–17	0.18	8.39E–06	0.3568

[a] S_r is the residual liquid-phase saturation (not in situ saturation).

[b] α and m are fitting parameters for capillary pressure and relative permeability curves, respectively.

Table 2-12. Fracture property values November 1997 TH and December 1997 modified-TH hydrologic parameter sets (Hardin et al., 1998)

Geologic unit	Model unit	Porosity	Permeability (m^2)		S_r [a]	α (Pa^{-1}) [b]	m [b]	FMX
			Vertical	Horizontal				
Tpcp11	tcw11	2.33E–04	2.29E–11	6.03E–12	0.01	2.37E–03	0.667	5.00E–04
Tpcpln	tcw12	2.99E–04	1.38E–11	6.03E–12	0.01	2.37E–03	0.669	5.00E–04
Tpcpv	tcw13	7.05E–05	2.82E–12	2.40E–13	0.01	9.12E–04	0.669	5.00E–04
Tpcpv1	ptn21	4.84E–05	5.25E–13	5.25E–13	0.01	1.10E–03	0.669	5.02E–01
Tpy	ptn22	4.83E–05	1.95E–13	1.95E–13	0.01	1.85E–03	0.669	5.00E–01
Tpbt3	ptn23	1.30E–04	2.57E–13	2.57E–13	0.01	3.45E–03	0.667	5.00E–01
Tpp	ptn24	6.94E–05	6.17E–14	6.17E–14	0.01	9.13E–04	0.667	5.00E–01
Tpbt2	ptn25	3.86E–05	7.76E–14	7.76E–14	0.10	1.81E–04	0.320	5.00E–01
Tptrv	tsw31	8.92E–05	1.07E–11	1.00E–12	0.01	1.44E–04	0.566	4.68E–01
Tptrn	tsw32	1.29E–04	1.51E–11	7.08E–13	0.01	1.42E–03	0.667	5.00E–04
Tptpul	tsw33	1.05E–04	2.63E–11	8.91E–13	0.01	1.73E–03	0.667	5.00E–04
Tptpmn	tsw34	1.24E–04	6.76E–12	4.27E–13	0.01	9.34E–04	0.643	1.23E–03
Tptp11	tsw35	3.29E–04	3.80E–12	9.12E–13	0.01	1.26E–03	0.667	5.00E–04
Tptpln	tsw36	3.99E–04	1.20E–12	1.20E–12	0.01	1.32E–03	0.667	5.00E–04
Tptpv	tsw37	4.92E–04	1.20E–12	1.20E–12	0.01	1.19E–03	0.659	5.00E–04
Tpbt1	ch1zc	1.10E–05	2.51E–14	2.40E–14	0.01	1.14E–03	0.667	5.00E–01
Tac(z)	ch2zc	1.10E–05	2.51E–14	1.17E–14	0.01	1.12E–03	0.654	9.22E–01
Tac(z)	ch3zc	1.10E–05	2.51E–14	1.17E–14	0.01	1.12E–03	0.654	9.22E–01
Tacbt	ch4zc	1.10E–05	2.51E–14	1.55E–14	0.01	1.14E–03	0.667	5.00E–01
Tpbt1	ch1vc	7.14E–05	1.74E–13	1.74E–13	0.01	1.18E–03	0.669	5.00E–01
Tac(v)	ch2vc	7.14E–05	2.88E–13	2.88E–13	0.01	1.18E–03	0.667	5.00E–01
Tac(v)	ch3vc	7.14E–05	2.88E–13	2.88E–13	0.01	1.18E–03	0.667	5.00E–01
Tabt1	ch4vc	7.14E–05	2.88E–13	2.88E–13	0.01	1.18E–03	0.667	5.00E–01
Tcp(3)	pp3vp	7.14E–05	7.08E–13	6.92E–13	0.01	1.42E–03	0.667	5.00E–04
Tcb(w)	bf3vb	7.14E–05	7.08E–13	6.92E–13	0.01	1.42E–03	0.667	5.00E–04
Tcb(w)	tm3vt	7.14E–05	7.08E–13	6.92E–13	0.01	1.42E–03	0.667	5.00E–04
Tcp(2)	pp2zp	1.10E–05	2.51E–14	6.46E–14	0.01	1.14E–03	0.667	5.00E–01
Tcb(n)	bf2zb	1.10E–05	2.51E–14	6.46E–14	0.01	1.14E–03	0.667	5.00E–01

[a] S_r is the residual liquid-phase saturation (not in situ saturation).

[b] α and m are fitting parameters for capillary pressure and relative permeability curves, respectively.

Table 2-13. Matrix property values for the December 1997 modified-TH hydrologic parameter set for only the values that differ from the November 1997 TH hydrologic parameter set (Hardin et al., 1998)

The December 1997 modified-TH set was modified from the November 1997 TH set on the basis of imbibition sorptivity measurements by Flint et al. (1996b).

Geologic unit	Model unit	Porosity	Permeability (m^2)	S_r [a]	α (Pa^{-1}) [b]	m [b]
Tptpln	tsw36	0.092	8.70E–18	0.18	2.272E–6	0.5138
Tptpv	tsw37	0.02	4.080E–18	0.5	7.3856E–6	0.3709

[a] S_r is the residual liquid-phase saturation (not in situ saturation).

[b] α and m are fitting parameters for capillary pressure and relative permeability curves, respectively.

Table 2-14. Fracture property values in the TSPA-VA base-case (December 1997) hydrologic parameter set for $I \times 1$ $\alpha_{f,mean}$ (CRWMS M&O, 1998)

Geologic unit	Model unit	Porosity	Permeability (m^2)		S_r [a]	α (Pa^{-1}) [b]	m [b]	FMX
			Vertical	Horizontal				
Tpcp11	tcw11	2.33E–04	2.29E–11	6.03E–12	0.01	2.53E–03	0.492	8.00E–03
Tpcpln	tcw12	2.99E–04	1.38E–11	6.03E–12	0.01	2.02E–03	0.492	8.00E–03
Tpcpv	tcw13	7.05E–05	2.82E–12	2.40E–13	0.01	8.10E–04	0.492	8.00E–03
Tpcpv1	ptn21	4.84E–05	5.25E–13	5.25E–13	0.01	1.31E–03	0.492	8.36E–01
Tpy	ptn22	4.83E–05	1.95E–13	1.95E–13	0.01	9.42E–04	0.492	8.36E–01
Tpbt3	ptn23	1.30E–04	2.57E–13	2.57E–13	0.01	1.03E–03	0.492	8.36E–01
Tpp	ptn24	6.94E–05	6.17E–14	6.17E–14	0.01	6.42E–04	0.492	8.36E–01
Tpbt2	ptn25	3.86E–05	7.76E–14	7.76E–14	0.01	6.93E–04	0.279	8.36E–01
Tptrv	tsw31	8.92E–05	1.07E–11	1.00E–12	0.01	3.98E–05	0.481	5.00E–01
Tptrn	tsw32	1.29E–04	1.51E–11	7.08E–13	0.01	1.18E–03	0.488	8.00E–03
Tptpul	tsw33	1.05E–04	2.63E–11	8.91E–13	0.01	1.40E–03	0.492	8.00E–03
Tptpmn	tsw34	1.24E–04	6.76E–12	4.27E–13	0.01	8.36E–04	0.492	8.00E–03
Tptp11	tsw35	3.29E–04	3.80E–12	9.12E–13	0.01	1.41E–03	0.492	8.00E–03
Tptpln	tsw36	3.99E–04	1.20E–12	1.20E–12	0.01	1.18E–03	0.492	8.00E–03
Tptpv	tsw37	4.92E–04	1.20E–12	1.20E–12	0.01	1.21E–03	0.492	8.00E–03
Tpbt1	ch1zc	1.10E–05	2.51E–14	2.40E–14	0.01	4.76E–04	0.492	1.00E+00
Tac(z)	ch2zc	1.10E–05	2.51E–14	1.17E–14	0.01	4.76E–04	0.492	1.00E+00
Tac(z)	ch3zc	1.10E–05	2.51E–14	1.17E–14	0.01	4.76E–04	0.492	1.00E+00
Tacbt	ch4zc	1.10E–05	2.51E–14	1.55E–14	0.01	4.76E–04	0.492	1.00E+00
Tpbt1	ch1vc	7.14E–05	1.74E–13	1.74E–13	0.01	9.07E–04	0.492	8.36E–01
Tac(v)	ch2vc	7.14E–05	2.88E–13	2.88E–13	0.01	9.07E–04	0.492	8.36E–01
Tac(v)	ch3vc	7.14E–05	2.88E–13	2.88E–13	0.01	9.07E–04	0.492	8.36E–01
Tabt1	ch4vc	7.14E–05	2.88E–13	2.88E–13	0.01	9.07E–04	0.492	8.36E–01
Tcp(3)	pp3vp	7.14E–05	7.08E–13	6.92E–13	0.01	1.18E–03	0.492	8.00E–03
Tcb(w)	bf3vb	7.14E–05	7.08E–13	6.92E–13	0.01	1.18E–03	0.492	8.00E–03

Geologic unit	Model unit	Porosity	Permeability (m^2)		S_r [a]	α (Pa^{-1}) [b]	m [b]	FMX
			Vertical	Horizontal				
Tcb(w)	tm3vt	7.14E–05	7.08E–13	6.92E–13	0.01	1.18E–03	0.492	8.00E–03
Tcp(2)	pp2zp	1.10E–05	2.51E–14	6.46E–14	0.01	4.76E–04	0.492	1.00E+00
Tcb(n)	bf2zb	1.10E–05	2.51E–14	6.46E–14	0.01	4.76E–04	0.492	1.00E+00

[a] S_r is the residual liquid-phase saturation (not in situ saturation).

[b] α and m are fitting parameters for capillary pressure and relative permeability curves, respectively.

Table 2-15. Fracture property values in the TSPA-VA base-case (12/97) hydrologic parameter set for $I \times 3\ \alpha_{f,max}$ (CRWMS M&O, 1998)

Geologic unit	Model unit	Porosity	Permeability (m^2)		S_r [a]	α (Pa^{-1}) [b]	m [b]	FMX
			Vertical	Horizontal				
Tpcp11	tcw11	2.33E–04	2.29E–11	6.03E–12	0.01	1.02E–02	0.492	4.62E–05
Tpcpln	tcw12	2.99E–04	1.38E–11	6.03E–12	0.01	7.49E–03	0.492	4.62E–05
Tpcpv	tcw13	7.05E–05	2.82E–12	2.40E–13	0.01	1.11E–03	0.492	4.62E–05
Tpcpv1	ptn21	4.84E–05	5.25E–13	5.25E–13	0.01	2.80E–03	0.492	4.02E–03
Tpy	ptn22	4.83E–05	1.95E–13	1.95E–13	0.01	3.09E–03	0.492	4.02E–03
Tpbt3	ptn23	1.30E–04	2.57E–13	2.57E–13	0.01	1.65E–03	0.492	4.02E–03
Tpp	ptn24	6.94E–05	6.17E–14	6.17E–14	0.01	1.67E–03	0.492	4.02E–03
Tpbt2	ptn25	3.86E–05	7.76E–14	7.76E–14	0.01	1.10E–03	0.279	4.02E–03
Tptrv	tsw31	8.92E–05	1.07E–11	1.00E–12	0.01	3.98E–05	0.481	5.00E–01
Tptrn	tsw32	1.29E–04	1.51E–11	7.08E–13	0.01	5.42E–03	0.488	4.62E–05
Tptpul	tsw33	1.05E–04	2.63E–11	8.91E–13	0.01	6.78E–03	0.492	4.62E–05
Tptpmn	tsw34	1.24E–04	6.76E–12	4.27E–13	0.01	3.16E–03	0.492	4.62E–05
Tptp11	tsw35	3.29E–04	3.80E–12	9.12E–13	0.01	5.59E–03	0.492	4.62E–05
Tptpln	tsw36	3.99E–04	1.20E–12	1.20E–12	0.01	3.19E–03	0.492	4.62E–05
Tptpv	tsw37	4.92E–04	1.20E–12	1.20E–12	0.01	2.00E–03	0.492	4.62E–05
Tpbt1	ch1zc	1.10E–05	2.51E–14	2.40E–14	0.01	7.58E–04	0.492	1.00E+00
Tac(z)	ch2zc	1.10E–05	2.51E–14	1.17E–14	0.01	7.58E–04	0.492	1.00E+00
Tac(z)	ch3zc	1.10E–05	2.51E–14	1.17E–14	0.01	7.58E–04	0.492	1.00E+00
Tacbt	ch4zc	1.10E–05	2.51E–14	1.55E–14	0.01	7.58E–04	0.492	1.00E+00
Tpbt1	ch1vc	7.14E–05	1.74E–13	1.74E–13	0.01	1.44E–03	0.492	4.02E–03
Tac(v)	ch2vc	7.14E–05	2.88E–13	2.88E–13	0.01	1.44E–03	0.492	4.02E–03
Tac(v)	ch3vc	7.14E–05	2.88E–13	2.88E–13	0.01	1.44E–03	0.492	4.02E–03
Tabt1	ch4vc	7.14E–05	2.88E–13	2.88E–13	0.01	1.44E–03	0.492	4.02E–03
Tcp(3)	pp3vp	7.14E–05	7.08E–13	6.92E–13	0.01	5.42E–03	0.492	4.62E–05
Tcb(w)	bf3vb	7.14E–05	7.08E–13	6.92E–13	0.01	5.42E–03	0.492	4.62E–05
Tcb(w)	tm3vt	7.14E–05	7.08E–13	6.92E–13	0.01	5.42E–03	0.492	4.62E–05
Tcp(2)	pp2zp	1.10E–05	2.51E–14	6.46E–14	0.01	7.58E–04	0.492	1.00E+00
Tcb(n)	bf2zb	1.10E–05	2.51E–14	6.46E–14	0.01	7.58E–04	0.492	1.00E+00

[a] S_r is the residual liquid-phase saturation (not in situ saturation).

[b] α and m are fitting parameters for capillary pressure and relative permeability curves, respectively.

Table 2-16. Fracture property values in the TSPA-VA base-case (12/97) hydrologic parameter set for $I \times 3\ \alpha_{f,min}$ (CRWMS M&O, 1998)

Geologic unit	Model unit	Porosity	Permeability (m^2)		S_r [a]	α (Pa^{-1}) [b]	m [b]	FMX
			Vertical	Horizontal				
Tpcp11	tcw11	2.33E–04	2.29E–11	6.03E–12	0.01	5.73E–04	0.492	4.75E–04
Tpcpln	tcw12	2.99E–04	1.38E–11	6.03E–12	0.01	4.88E–04	0.492	4.75E–04
Tpcpv	tcw13	7.05E–05	2.82E–12	2.40E–13	0.01	5.67E–04	0.492	4.75E–04
Tpcpv1	ptn21	4.84E–05	5.25E–13	5.25E–13	0.01	5.85E–04	0.492	5.46E–03
Tpy	ptn22	4.83E–05	1.95E–13	1.95E–13	0.01	2.74E–04	0.492	5.46E–03
Tpbt3	ptn23	1.30E–04	2.57E–13	2.57E–13	0.01	6.18E–04	0.492	5.46E–03
Tpp	ptn24	6.94E–05	6.17E–14	6.17E–14	0.01	2.35E–04	0.492	5.46E–03
Tpbt2	ptn25	3.86E–05	7.76E–14	7.76E–14	0.01	4.14E–04	0.279	5.46E–03
Tptrv	tsw31	8.92E–05	1.07E–11	1.00E–12	0.01	3.98E–05	0.481	5.00E–01
Tptrn	tsw32	1.29E–04	1.51E–11	7.08E–13	0.01	2.53E–04	0.488	4.75E–04
Tptpul	tsw33	1.05E–04	2.63E–11	8.91E–13	0.01	2.76E–04	0.492	4.75E–04
Tptpmn	tsw34	1.24E–04	6.76E–12	4.27E–13	0.01	1.98E–04	0.492	4.75E–04
Tptp11	tsw35	3.29E–04	3.80E–12	9.12E–13	0.01	3.40E–04	0.492	4.75E–04
Tptpln	tsw36	3.99E–04	1.20E–12	1.20E–12	0.01	3.92E–04	0.492	4.75E–04
Tptpv	tsw37	4.92E–04	1.20E–12	1.20E–12	0.01	5.77E–04	0.492	4.75E–04
Tpbt1	ch1zc	1.10E–05	2.51E–14	2.40E–14	0.01	2.85E–04	0.492	1.00E+00
Tac(z)	ch2zc	1.10E–05	2.51E–14	1.17E–14	0.01	2.85E–04	0.492	1.00E+00
Tac(z)	ch3zc	1.10E–05	2.51E–14	1.17E–14	0.01	2.85E–04	0.492	1.00E+00
Tacbt	ch4zc	1.10E–05	2.51E–14	1.55E–14	0.01	2.85E–04	0.492	1.00E+00
Tpbt1	ch1vc	7.14E–05	1.74E–13	1.74E–13	0.01	5.42E–04	0.492	5.46E–03
Tac(v)	ch2vc	7.14E–05	2.88E–13	2.88E–13	0.01	5.42E–04	0.492	5.46E–03
Tac(v)	ch3vc	7.14E–05	2.88E–13	2.88E–13	0.01	5.42E–04	0.492	5.46E–03
Tabt1	ch4vc	7.14E–05	2.88E–13	2.88E–13	0.01	5.42E–04	0.492	5.46E–03
Tcp(3)	pp3vp	7.14E–05	7.08E–13	6.92E–13	0.01	2.53E–04	0.492	4.75E–04
Tcb(w)	bf3vb	7.14E–05	7.08E–13	6.92E–13	0.01	2.53E–04	0.492	4.75E–04
Tcb(w)	tm3vt	7.14E–05	7.08E–13	6.92E–13	0.01	2.53E–04	0.492	4.75E–04
Tcp(2)	pp2zp	1.10E–05	2.51E–14	6.46E–14	0.01	2.85E–04	0.492	1.00E+00
Tcb(n)	bf2zb	1.10E–05	2.51E–14	6.46E–14	0.01	2.85E–04	0.492	1.00E+00

[a] S_r is the residual liquid-phase saturation (not in situ saturation).

[b] α and m are fitting parameters for capillary pressure and relative permeability curves, respectively.

Table 2-17. Fracture property values in the TSPA-VA base-case (12/97) hydrologic parameter set for $I \times 0.33\ \alpha_{f,max}$ (CRWMS M&O, 1998)

Geologic unit	Model unit	Porosity	Permeability (m^2)		S_r [a]	α (Pa^{-1}) [b]	m [b]	FMX
			Vertical	Horizontal				
Tpcp11	tcw11	2.33E–04	2.29E–11	6.03E–12	0.01	1.02E–02	0.492	5.03E–02
Tpcpln	tcw12	2.99E–04	1.38E–11	6.03E–12	0.01	7.49E–03	0.492	5.03E–02
Tpcpv	tcw13	7.05E–05	2.82E–12	2.40E–13	0.01	1.11E–03	0.492	5.03E–02
Tpcpv1	ptn21	4.84E–05	5.25E–13	5.25E–13	0.01	2.80E–03	0.492	8.98E–01
Tpy	ptn22	4.83E–05	1.95E–13	1.95E–13	0.01	3.09E–03	0.492	8.98E–01
Tpbt3	ptn23	1.30E–04	2.57E–13	2.57E–13	0.01	1.65E–03	0.492	8.98E–01
Tpp	ptn24	6.94E–05	6.17E–14	6.17E–14	0.01	1.67E–03	0.492	8.98E–01
Tpbt2	ptn25	3.86E–05	7.76E–14	7.76E–14	0.01	1.10E–03	0.279	8.98E–01
Tptrv	tsw31	8.92E–05	1.07E–11	1.00E–12	0.01	3.98E–05	0.481	5.00E–01
Tptrn	tsw32	1.29E–04	1.51E–11	7.08E–13	0.01	5.42E–03	0.488	5.03E–02
Tptpul	tsw33	1.05E–04	2.63E–11	8.91E–13	0.01	6.78E–03	0.492	5.03E–02
Tptpmn	tsw34	1.24E–04	6.76E–12	4.27E–13	0.01	3.16E–03	0.492	5.03E–02
Tptp11	tsw35	3.29E–04	3.80E–12	9.12E–13	0.01	5.59E–03	0.492	5.03E–02
Tptpln	tsw36	3.99E–04	1.20E–12	1.20E–12	0.01	3.19E–03	0.492	5.03E–02
Tptpv	tsw37	4.92E–04	1.20E–12	1.20E–12	0.01	2.00E–03	0.492	5.03E–02
Tpbt1	ch1zc	1.10E–05	2.51E–14	2.40E–14	0.01	7.58E–04	0.492	1.00E+00
Tac(z)	ch2zc	1.10E–05	2.51E–14	1.17E–14	0.01	7.58E–04	0.492	1.00E+00
Tac(z)	ch3zc	1.10E–05	2.51E–14	1.17E–14	0.01	7.58E–04	0.492	1.00E+00
Tacbt	ch4zc	1.10E–05	2.51E–14	1.55E–14	0.01	7.58E–04	0.492	1.00E+00
Tpbt1	ch1vc	7.14E–05	1.74E–13	1.74E–13	0.01	1.44E–03	0.492	8.98E–01
Tac(v)	ch2vc	7.14E–05	2.88E–13	2.88E–13	0.01	1.44E–03	0.492	8.98E–01
Tac(v)	ch3vc	7.14E–05	2.88E–13	2.88E–13	0.01	1.44E–03	0.492	8.98E–01
Tabt1	ch4vc	7.14E–05	2.88E–13	2.88E–13	0.01	1.44E–03	0.492	8.98E–01
Tcp(3)	pp3vp	7.14E–05	7.08E–13	6.92E–13	0.01	5.42E–03	0.492	5.03E–02
Tcb(w)	bf3vb	7.14E–05	7.08E–13	6.92E–13	0.01	5.42E–03	0.492	5.03E–02
Tcb(w)	tm3vt	7.14E–05	7.08E–13	6.92E–13	0.01	5.42E–03	0.492	5.03E–02
Tcp(2)	pp2zp	1.10E–05	2.51E–14	6.46E–14	0.01	7.58E–04	0.492	1.00E+00
Tcb(n)	bf2zb	1.10E–05	2.51E–14	6.46E–14	0.01	7.58E–04	0.492	1.00E+00

[a] S_r is the residual liquid-phase saturation (not in situ saturation).

[b] α and m are fitting parameters for capillary pressure and relative permeability curves, respectively.

Table 2-18. Fracture property values in the TSPA-VA base-case (12/97) hydrologic parameter set for $I \times 0.33\ \alpha_{f,min}$ (CRWMS M&O, 1998)

Geologic unit	Model unit	Porosity	Permeability (m^2)		S_r [a]	α (Pa^{-1}) [b]	m [b]	FMX
			Vertical	Horizontal				
Tpcp11	tcw11	2.33E–04	2.29E–11	6.03E–12	0.01	5.73E–04	0.492	1.90E–01
Tpcpln	tcw12	2.99E–04	1.38E–11	6.03E–12	0.01	4.88E–04	0.492	1.90E–01
Tpcpv	tcw13	7.05E–05	2.82E–12	2.40E–13	0.01	5.67E–04	0.492	1.90E–01
Tpcpv1	ptn21	4.84E–05	5.25E–13	5.25E–13	0.01	5.85E–04	0.492	1.00E+00
Tpy	ptn22	4.83E–05	1.95E–13	1.95E–13	0.01	2.74E–04	0.492	1.00E+00
Tpbt3	ptn23	1.30E–04	2.57E–13	2.57E–13	0.01	6.18E–04	0.492	1.00E+00
Tpp	ptn24	6.94E–05	6.17E–14	6.17E–14	0.01	2.35E–04	0.492	1.00E+00
Tpbt2	ptn25	3.86E–05	7.76E–14	7.76E–14	0.01	4.14E–04	0.279	1.00E+00
Tptrv	tsw31	8.92E–05	1.07E–11	1.00E–12	0.01	3.98E–05	0.481	5.00E–01
Tptrn	tsw32	1.29E–04	1.51E–11	7.08E–13	0.01	2.53E–04	0.488	1.90E–01
Tptpul	tsw33	1.05E–04	2.63E–11	8.91E–13	0.01	2.76E–04	0.492	1.90E–01
Tptpmn	tsw34	1.24E–04	6.76E–12	4.27E–13	0.01	1.98E–04	0.492	1.90E–01
Tptp11	tsw35	3.29E–04	3.80E–12	9.12E–13	0.01	3.40E–04	0.492	1.90E–01
Tptpln	tsw36	3.99E–04	1.20E–12	1.20E–12	0.01	3.92E–04	0.492	1.90E–01
Tptpv	tsw37	4.92E–04	1.20E–12	1.20E–12	0.01	5.77E–04	0.492	1.90E–01
Tpbt1	ch1zc	1.10E–05	2.51E–14	2.40E–14	0.01	2.85E–04	0.492	1.00E+00
Tac(z)	ch2zc	1.10E–05	2.51E–14	1.17E–14	0.01	2.85E–04	0.492	1.00E+00
Tac(z)	ch3zc	1.10E–05	2.51E–14	1.17E–14	0.01	2.85E–04	0.492	1.00E+00
Tacbt	ch4zc	1.10E–05	2.51E–14	1.55E–14	0.01	2.85E–04	0.492	1.00E+00
Tpbt1	ch1vc	7.14E–05	1.74E–13	1.74E–13	0.01	5.42E–04	0.492	1.00E+00
Tac(v)	ch2vc	7.14E–05	2.88E–13	2.88E–13	0.01	5.42E–04	0.492	1.00E+00
Tac(v)	ch3vc	7.14E–05	2.88E–13	2.88E–13	0.01	5.42E–04	0.492	1.00E+00
Tabt1	ch4vc	7.14E–05	2.88E–13	2.88E–13	0.01	5.42E–04	0.492	1.00E+00
Tcp(3)	pp3vp	7.14E–05	7.08E–13	6.92E–13	0.01	2.53E–04	0.492	1.90E–01
Tcb(w)	bf3vb	7.14E–05	7.08E–13	6.92E–13	0.01	2.53E–04	0.492	1.90E–01
Tcb(w)	tm3vt	7.14E–05	7.08E–13	6.92E–13	0.01	2.53E–04	0.492	1.90E–01
Tcp(2)	pp2zp	1.10E–05	2.51E–14	6.46E–14	0.01	2.85E–04	0.492	1.00E+00
Tcb(n)	bf2zb	1.10E–05	2.51E–14	6.46E–14	0.01	2.85E–04	0.492	1.00E+00

[a] S_r is the residual liquid-phase saturation (not in situ saturation).

[b] α and m are fitting parameters for capillary pressure and relative permeability curves, respectively.

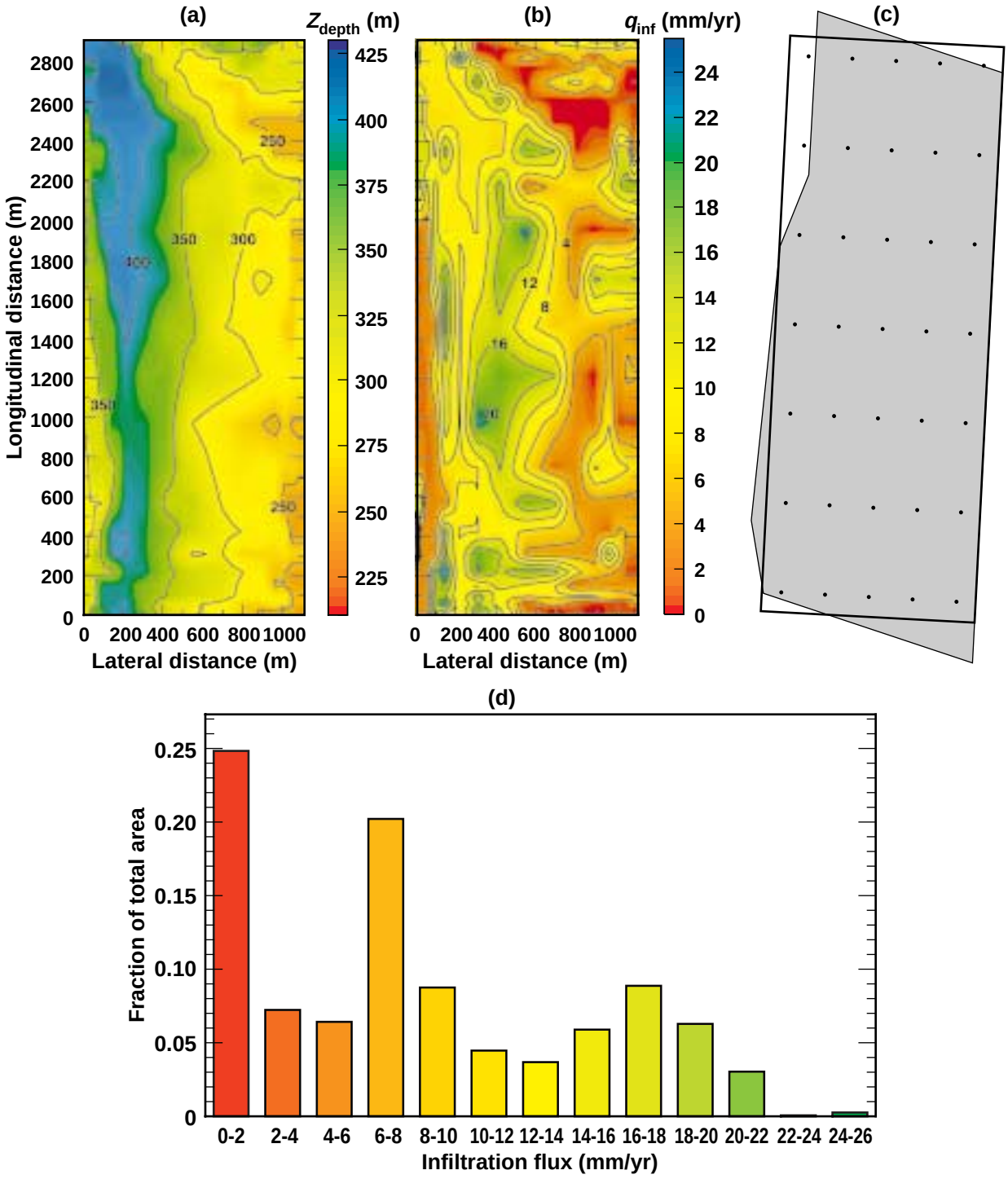

Figure 2-1. Surface topography, shallow infiltration, repository footprint, and model domain for site-scale thermal modeling at Yucca Mountain (a) depth of repository horizon below ground surface (b) infiltration-flux distribution over the approximate repository region (c) submodel locations on actual repository region and (d) frequency histogram for infiltration flux, corresponding to the contour map of (b)

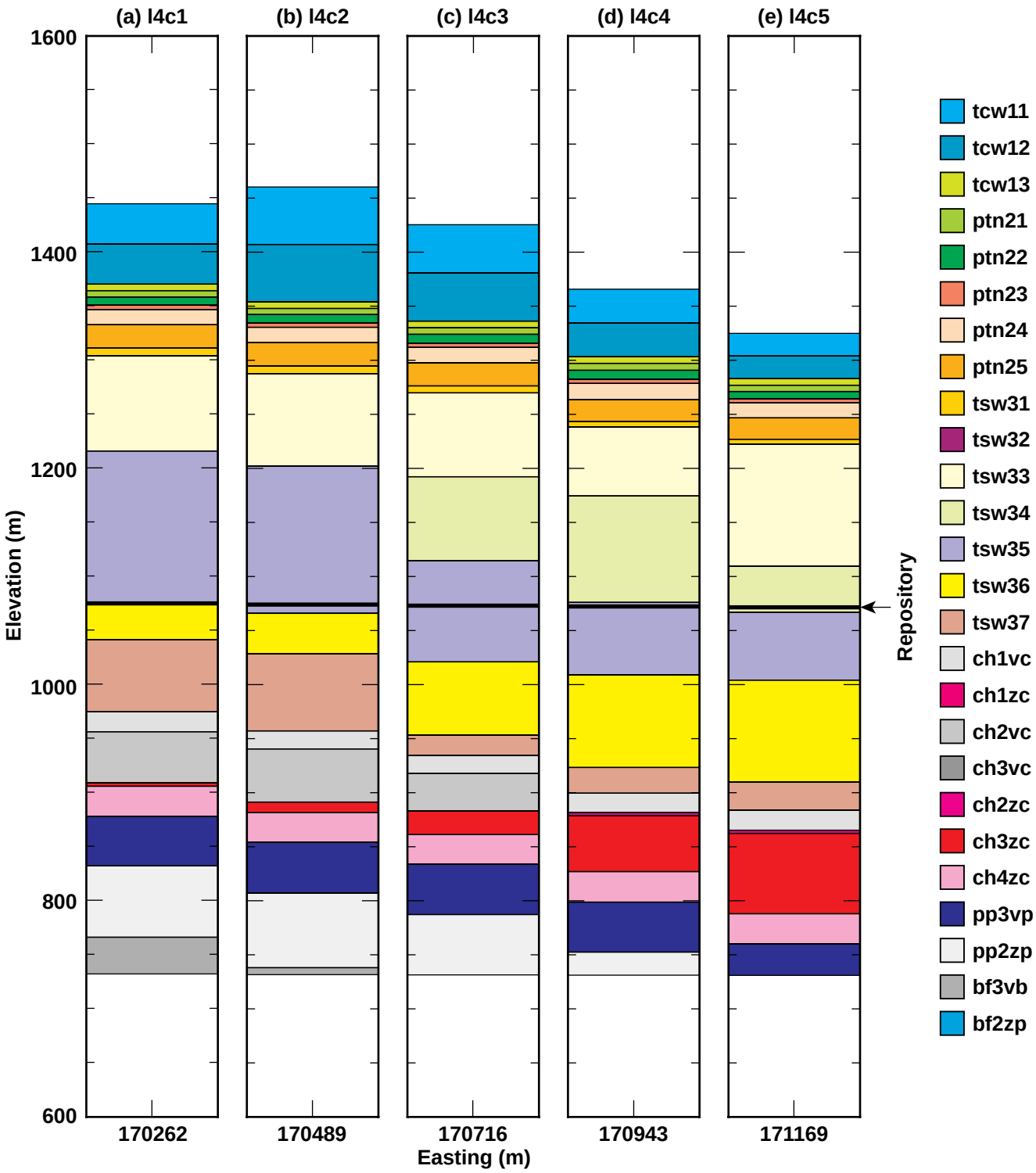

Figure 2-2.. Vertical distribution of hydrostratigraphic model units shown for drift-scale model locations (in Nevada-State coordinates) (columns l4c1–l4c5)

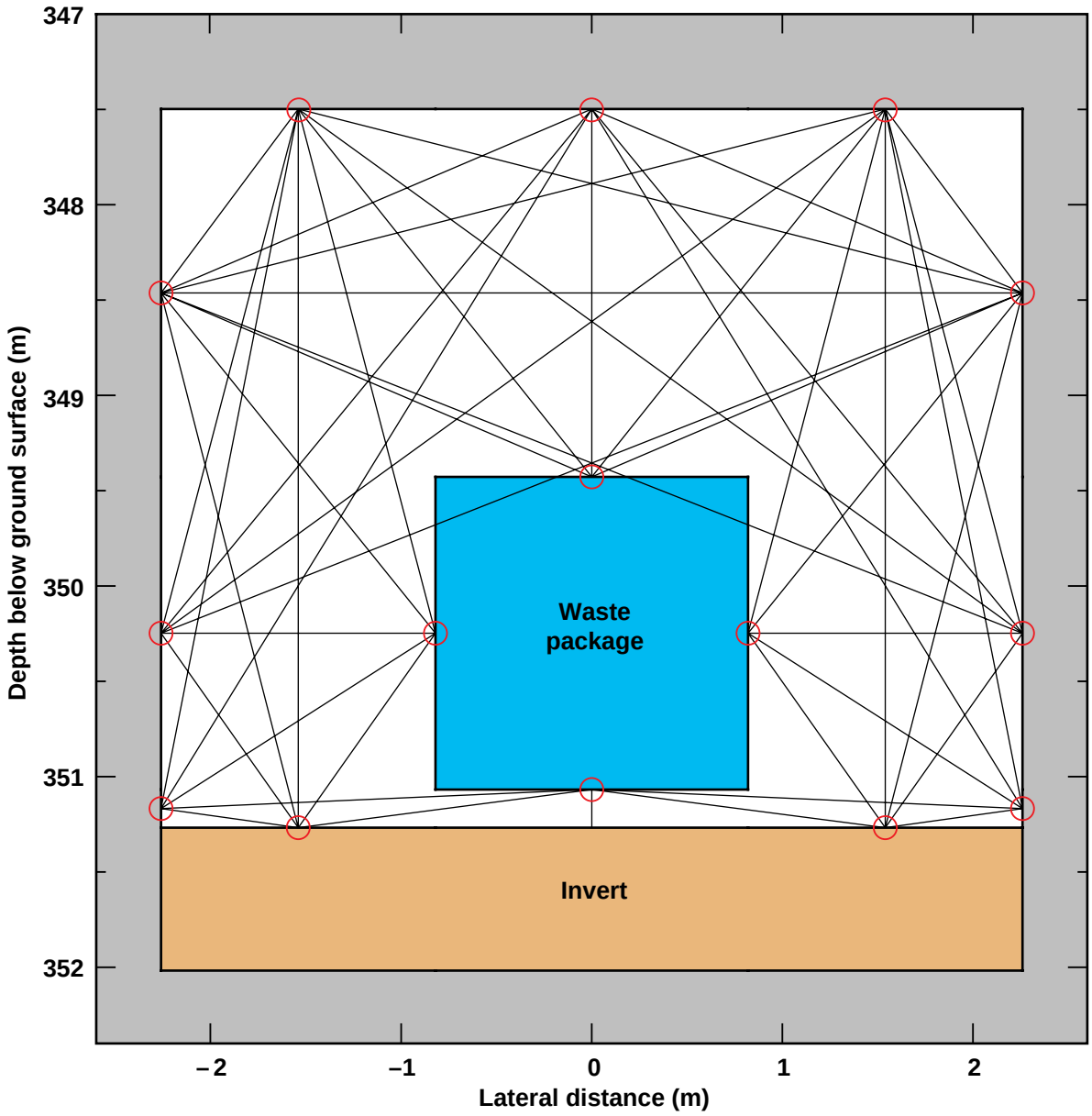

Figure 2-3. Vertical cross-section of the emplacement drift in the DDT and LDTH models, showing the thermal-radiation connections among the surfaces in the drift that are used in thermal simulations

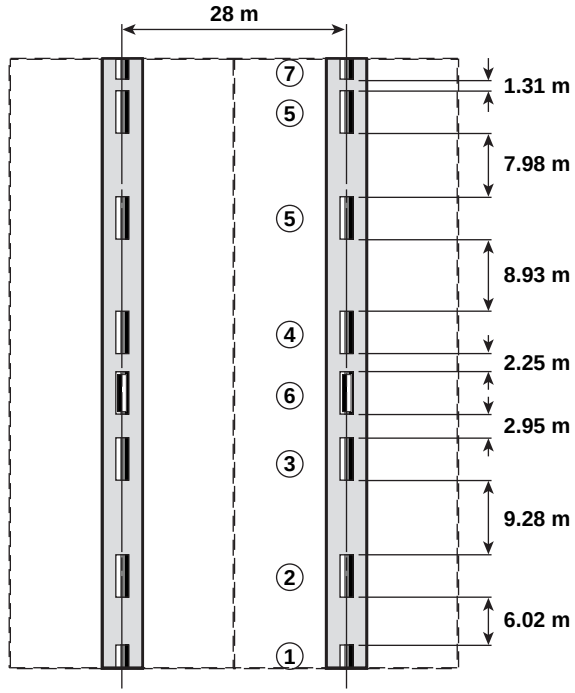

(b) Line-load design, LML = 1.189 MTU/m

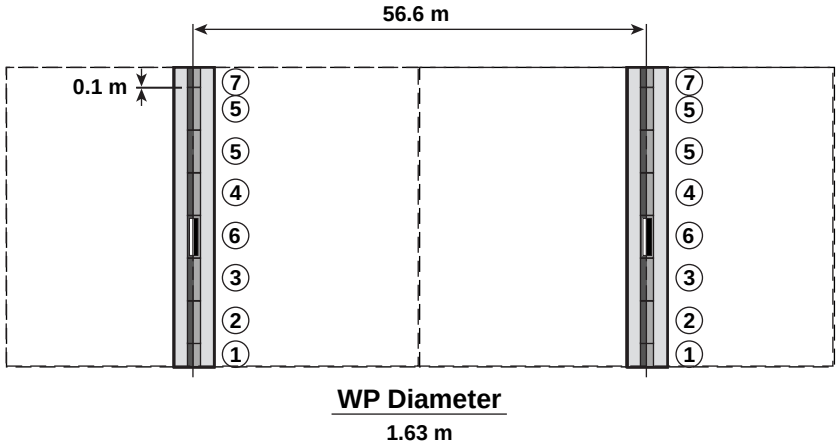

Legend						
①	②	③	④	⑤	⑥	⑦
12 PWR	21 PWR	21 PWR	21 PWR	2x44 PWR	Co-Disposal	Direct-Disposal
(1/2) 6.25 MTU (1/2) 10.48 kW (1/2) 5.87 m	7.4 MTU 2.91 kW 5.3 m	9.4 MTU 17.85 kW 5.3 m	8.93 MTU 9.34 kW 5.3 m	7.81 MTU 6.44 kW 5.3 m	4.06 kW 5.37 m	(1/2) 0.793 kW (1/2) 5.37 m

Figure 2-4. Plan view of the WP layout represented in the DDT models

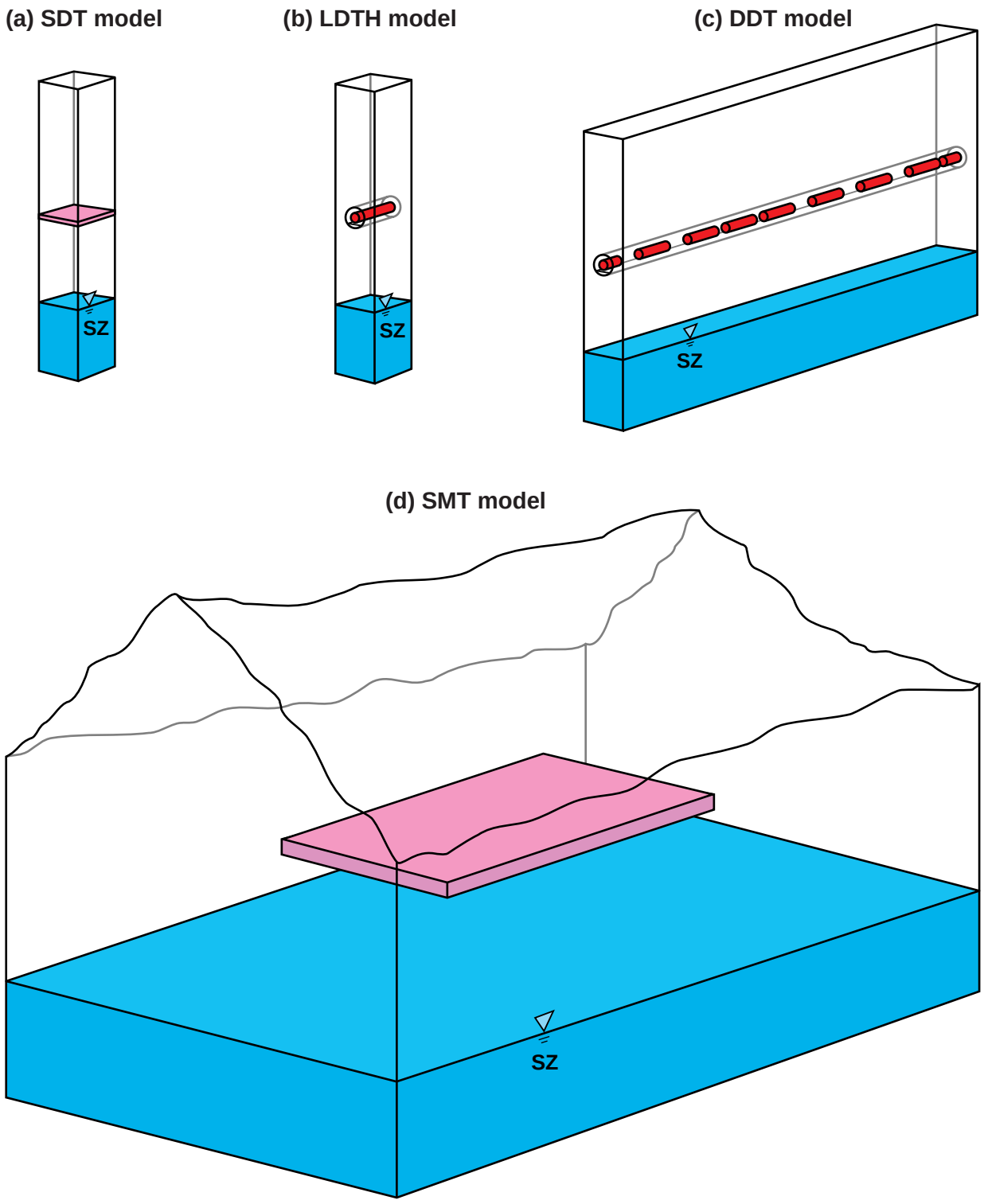

Figure 2-5. Schematic of conceptual models used by the multiscale TH modeling approach

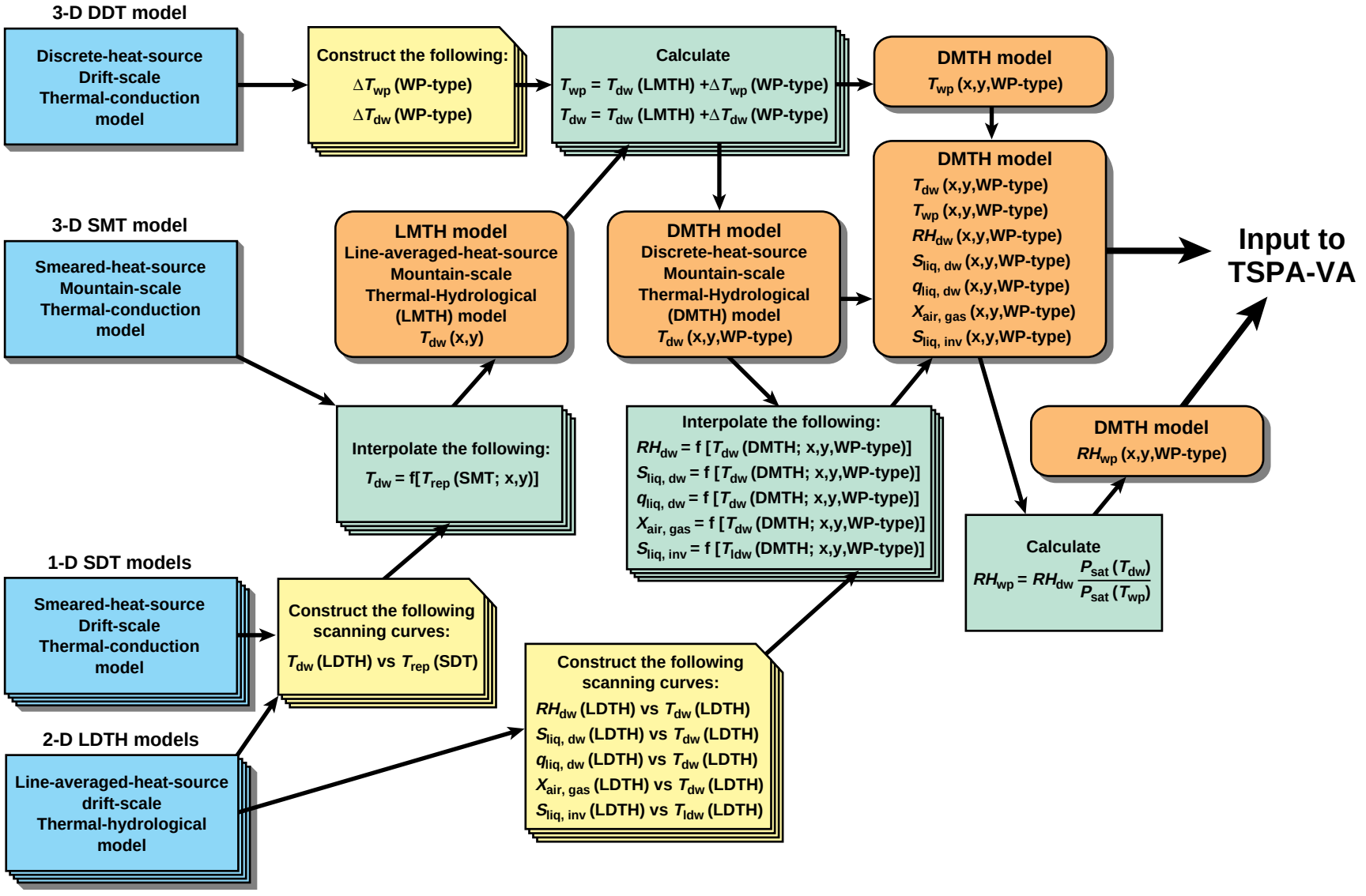

Figure 2-6. Flow chart for the multiscale TH modeling approach for (a) cases with no engineered backfill (Hardin 1998)

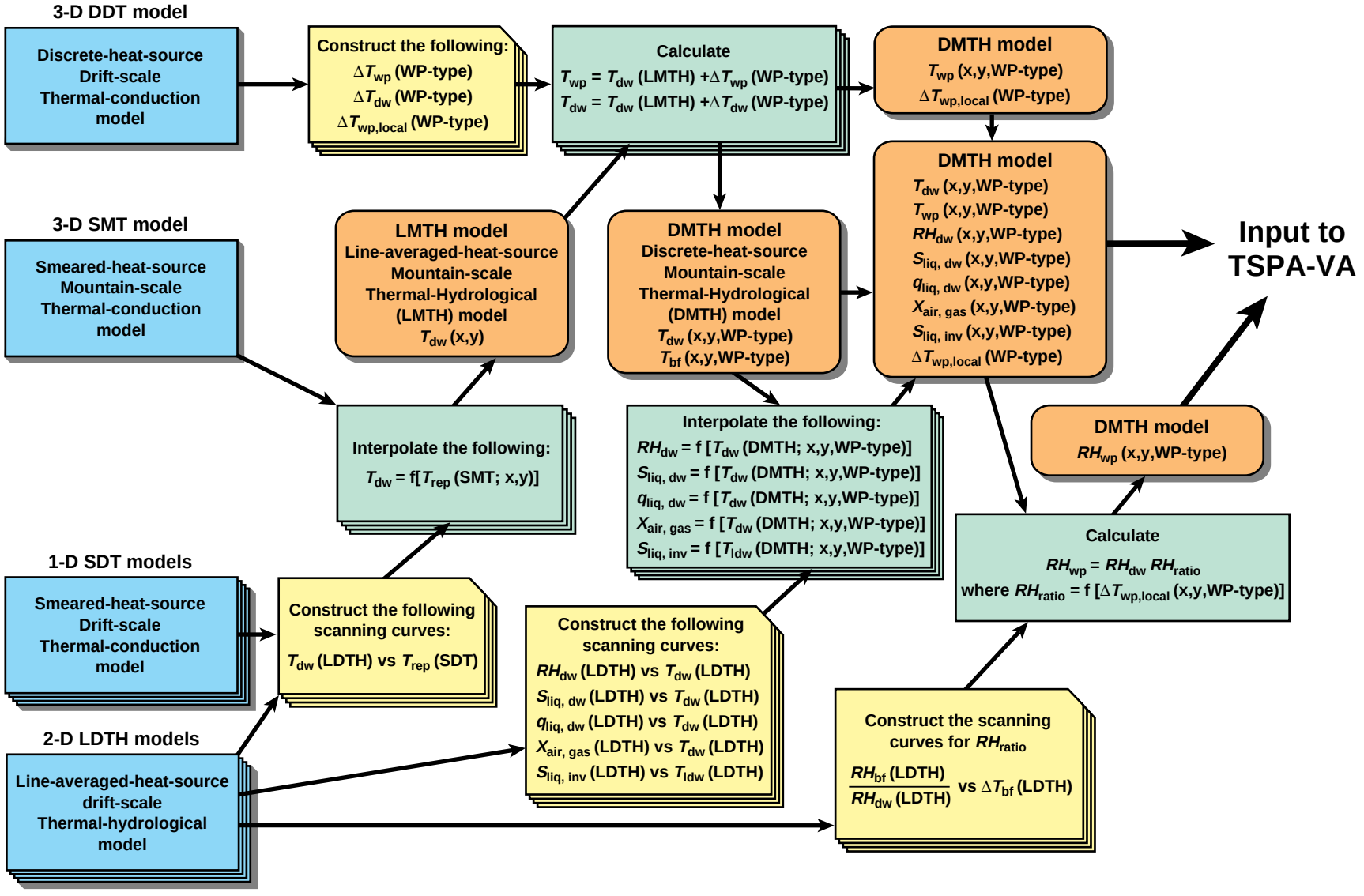

Figure 2-6. Flow chart for the multiscale TH modeling approach for (b) cases with engineered backfill (Hardin 1998)

3. Model Results

Three key thermohydrologic concerns for EBS performance assessment are

- The magnitude and distribution of decay-heat-mobilized liquid-phase flux and the influence of that flux on seepage into emplacement drifts
- The spatial and temporal extent of rock dryout and relative humidity *RH* reduction
- The influence of rock dryout and convective heat-flow (e.g., the heat-pipe effect) on temperatures in the near field and in the EBS (and on WPs)

Rock dryout is the result of the balance between the rate of vaporization and vapor transport away from emplacement drifts and the rate of return liquid-phase flow to the dryout zone. Two mechanisms influence the rate of rewetting:

- Gravity-driven percolation and condensate flux in fractures
- Capillary-driven mechanisms
  - Matrix imbibition, as quantified by the matrix wetting diffusivity D_{imb}, which is defined in this section and discussed elsewhere (Buscheck et al., 1997).
  - Wicking in fractures, as quantified by $1/\alpha_f$, where α_f is the van Genuchten alpha parameter for fractures, which is equivalent to the air-entry (or bubble-point) pressure

The effectiveness of heat pipes strongly depends on whether gravity is the principal driving force for the return flow of condensate to the boiling zone or whether the return flow is substantially augmented by matrix imbibition and capillary wicking in fractures. For rewetting by fracture flow, gravity always plays a role at the boiling front lying above the repository horizon — so, if capillary wicking in fractures is substantial, it will add to the influence of gravity above the repository as well as constitute the major fracture-flow rewetting mechanism below the repository horizon. Because the matrix permeability of the host-rock units (see Tables 2-9, 2-11, and 2-13) is too small for gravity-driven drainage to be significant, matrix imbibition is the major mechanism for rewetting in the matrix.

The matrix-wetting diffusivity D_{imb} is a measure of the magnitude of matrix imbibition that contributes to rewetting the dryout zone back to ambient liquid-phase saturation conditions. The volumetric flux q_{imb} into a 1-D imbibition experiment is known to have the form

$$q_{imb} = \phi(S_s - S_i)\sqrt{D_{imb}/\pi t} \ , \qquad \text{(Eq. 3-1)}$$

where ϕ is porosity, S_s is satiated liquid-phase saturation, S_i is initial liquid-phase saturation, t is time, and D_{imb} is effective matrix-imbibition diffusivity defined by Nitao (1991). Nitao used the results of Zimmerman and Bodvarsson (1989) to write an approximate expression for the matrix diffusivity,

$$D_{imb} \approx \frac{\pi K_m}{2\phi\alpha(2-m)(S_s - S_i)}\left(\frac{1}{m}(1-\gamma)\right)^{1/n} \ , \qquad \text{(Eq. 3-2)}$$

where K_m is saturated matrix hydraulic conductivity, α and m are the matrix van Genuchten parameters, $n = 1/(m-1)$, and the normalized initial saturation $\gamma = (S_i - S_r)/(S_s - S_r)$.

Table 3-1 presents values of D_{imb} for the host-rock and nearby units for the parameter sets considered in this study.

Table 3-1. The value of matrix wetting diffusivity D_{imb} for the host-rock units and neighboring units, for various hydrologic parameter sets (m^2/sec) with an assumed S_{liq} of 90%

Host-rock model unit	7/97 TSPA-VA preliminary base-case and all 12/97 TSPA-VA base-case parameter sets	11/97 TH parameter set	12/97 modified-TH parameter set
tsw33	5.98E–08	1.15E–07	1.15E–07
tsw34	2.17E–07	1.86E–07	1.86E–07
tsw35	2.03E–07	2.65E–07	2.65E–07
tsw36	6.32E–06	5.33E–07	1.86E–07
tsw37	2.70E–06	5.23E–06	1.86E–07

Another important issue influencing dryout and heat pipes is the effectiveness of condensate drainage. The term condensate "shedding" is sometimes used to refer to condensate drainage that is not imbibed by the rock matrix in the immediately vicinity of the dryout zone. From a numerical modeling standpoint, it is important to represent how nonequilibrium fracture-matrix interaction influences condensate shedding. The equivalent continuum model (ECM) assumes instantaneous capillary-pressure equilibrium between the fractures and adjoining matrix blocks and thus tends to underpredict the tendency for condensate to shed away from the dryout zone surrounding emplacement drifts. The dual-permeability model (DKM) attempts to more realistically represent condensate shedding. Two factors in the DKM influence the tendency for condensate to shed:

- The magnitude of matrix imbibition, as quantified by D_{imb}, influences the tendency for condensate to be imbibed in the vicinity of the dryout zone. The efficiency of condensate shedding increases with decreasing D_{imb}.
- The channeling or "fingering" of condensate drainage pathways in the fracture network controls the fracture surface area that is exposed to fracture flow; this exposed area is the conduit for matrix imbibition. The FMX factor for liquid-phase interaction accounts for channeling of flow as the liquid phase "fingers" through the fracture network. If liquid-phase drainage in fractures is ubiquitous (as opposed to highly focused into a few fingers), FMX will be closer to unity. If liquid-phase drainage is channeled into a few predominant pathways (or fingers), FMX will be small.

3.1 Influence of Infiltration flux and Fracture Properties on EBS TH Conditions

The repository host-rock (i.e., the rock that contains the emplacement drifts) comprises three hydrogeologic model units across the entire repository area (**Figure 3-1**a and Table 2-2). Two of the host-rock units (tsw34 and tsw35) have similar matrix properties that result in a similar value of D_{imb} in the July 1997 TSPA-VA preliminary base-case and December 1997 base-case parameter sets (Table 3-1). The third host-rock unit (tsw36) has a much larger value of D_{imb}. Consequently, the tsw34 and tsw35 host-rock units result in similar rewetting behavior because of matrix imbibition, while the tsw36 results in a much greater tendency for matrix imbibition to rewet the dryout zone. In past studies (Buscheck et al., 1997), it was

shown that it is very useful to consider the distance from the repository horizon to the top of the tsw36 unit (Figure 3-1b) when analyzing the influence of matrix imbibition on rewetting and on EBS TH conditions.

Figure 3-1 Plan view of host-rock distribution

(a) shown for the SMT-model grid of the repository area as a function of Nevada-State coordinates

(b) contour map of the vertical distance $\Delta Z_{rep\text{-}tsw36}$ between the repository horizon and the top of the tsw36 hydrogeologic model unit shown as a function of distance from the southwest corner of the repository area in the SMT model, where the SMT model is the smeared-heat-source mountain-scale thermal model

For the December 1997 TSPA-VA base-case parameter set, there are minor differences in the values of α_f for the respective host-rock units (**Table 3-2**); within a given TSPA-VA parameter set, the FMX values are identical for the three host-rock units (**Table 3-3**). There are some differences in bulk permeability k_b (which primarily arises from fracture permeability) among the three host-rock units (Table 2-14); however, k_b is large enough in all three host-rock units for buoyant gas-phase convection to potentially significantly affect TH behavior. Earlier studies (e.g., Buscheck and Nitao, 1994) showed that the threshold value of k_b (above which buoyant gas-phase convection significantly influences vapor and heat flow) is about 1 to 5 darcy. The vertical component of k_b for the three host-rock units ranges from 1.2 darcy in the tsw36 to 6.7 darcy in the tsw34; the horizontal component of k_b ranges from 0.43 darcy in the tsw34 to 1.2 darcy in the tsw36. Therefore, the three host-rock units roughly straddle the threshold value of k_b for buoyant gas-phase convection to significantly affect TH behavior.

Table 3-2. The value of α_f for the host-rock units and neighboring units, for various hydrologic parameter sets, where α_f is the van Genuchten alpha parameter for fractures

		Host-rock model unit				
Hydrologic parameter set		**tsw33**	**tsw34**	**tsw35**	**tsw36**	**tsw37**
7/97 TSPA-VA preliminary base case		1.78E–04	9.77E–05	1.10E–04	1.32E–04	1.17E–04
11/97 TH and 12/97 modified-TH		1.73E–03	9.34E–04	1.26E–03	1.32E–03	1.19E–03
12/97 TSPA-VA base case	$I \times 1$ $\alpha_{f,mean}$	1.40E–03	8.36E–04	1.41E–03	1.18E–03	1.21E–03
	$I \times 3$ $\alpha_{f,max}$	6.78E–03	3.16E–03	5.59E–03	3.19E–03	2.00E–03
	$I \times 3$ $\alpha_{f,min}$	2.76E–04	1.98E–04	3.40E–04	3.92E–04	5.77E–04
	$I \times 0.33$ $\alpha_{f,max}$	6.78E–03	3.16E–03	5.59E–03	3.19E–03	2.00E–03
	$I \times 0.33$ $\alpha_{f,min}$	2.76E–04	1.98E–04	3.40E–04	3.92E–04	5.77E–04

Table 3-3. The value of FMX factor for the host-rock units and neighboring units, for various hydrologic parameter sets

		Host-rock model unit				
Hydrologic parameter set		**tsw33**	**tsw34**	**tsw35**	**tsw36**	**tsw37**
7/97 TSPA-VA preliminary base case		7.94E–05	1.55E–04	7.76E–02	4.79E–05	4.90E–04
11/97 TH and 12/97 modified-TH		5.00E–04	1.23E–03	5.00E–04	5.00E–04	5.00E–04
12/97 TSPA-VA base case	$I \times 1\ \alpha_{f,mean}$	8.00E–03	8.00E–03	8.00E–03	8.00E–03	8.00E–03
	$I \times 3\ \alpha_{f,max}$	4.62E–05	4.62E–05	4.62E–05	4.62E–05	4.62E–05
	$I \times 3\ \alpha_{f,min}$	4.75E–04	4.75E–04	4.75E–04	4.75E–04	4.75E–04
	$I \times 0.33\ \alpha_{f,max}$	5.03E–02	5.03E–02	5.03E–02	5.03E–02	5.03E–02
	$I \times 0.33\ \alpha_{f,min}$	1.90E–01	1.90E–01	1.90E–01	1.90E–01	1.90E–01

Another distinguishable characteristic of the three host-rock units is their respective values of wet and dry thermal conductivity K_{th} (Table 2-7). The wet values of K_{th} range from 1.84 W/m°C in the tsw36 to 2.33 W/m°C in the tsw34. The dry values of K_{th} range from 1.2 W/m°C in the tsw35 to 1.56 W/m°C in the tsw34. The larger values of wet and dry K_{th} in the tsw34 cause less near-field (and drift-wall) temperature increase along the eastern to south-eastern boundary of the repository where the tsw34 is the predominant host-rock unit; the greatest temperature increase occurs in the central portion of the repository where the tsw35 is the predominant host-rock unit.

The differences between the July 1997 TSPA-VA preliminary base-case parameter set and the December 1997 TSPA-VA base-case parameter set are confined to their respective values α_f , which is the van Genuchten alpha parameter for fractures (Table 3-2), and to their respective values of FMX (Table 3-3). The July 1997 TSPA preliminary base-case parameter set has values of α_f that are an order of magnitude smaller than those in the December 1997 TSPA-VA base-case set. Consequently, capillary wicking in fractures is about 10 times stronger in the July 1997 preliminary base-case set. The stronger fracture wicking resulting from the July 1997 preliminary base-case set causes stronger rewetting, which allows somewhat less rock dryout and *RH* reduction (compare **Figure 3-2**a and Figure 3-2d). **Figure 3-3**c and Figure 3-3d also show that *RH* reduction is less during the first 600 yr. The reduced extent of rock dryout results in slightly less near-field temperature increase in the July 1997 preliminary base-case (Figure 3-3a and Figure 3-3b) than it does in the December 1997 base case. Overall, the differences in temperature and *RH* between these two cases are small.

Figure 3-2. Relative humidity *RH* on the surface of "average" 21-PWR, medium-heat CSNF WPs at 1000 yr for the point-load design with no backfill

Curves are plotted for the following parameter sets and infiltration assumptions:

(a) December 1997 TSPA-VA base-case I x 1 $\alpha_{f,mean}$

b) December 1997 TSPA-VA base-case I x 0.33 $\alpha_{f,min}$

(c) December 1997 TSPA-VA base-case I x 3 $\alpha_{f,min}$

(d) July 1997 TSPA-VA preliminary base-case I x 1

(e) December 1997 TSPA-VA base-case I x 0.33 $\alpha_{f,max}$

(f) December 1997 TSPA-VA base-case I x 3 $\alpha_{f,max}$.

The symbol I stands for the nominal infiltration-flux q_{inf} map (average q_{inf} = 7.8 mm/yr) for the present-day climate, and α_f is the van Genuchten alpha parameter for fractures.

Figure 3-3. Summary of TH conditions are plotted for "average" 21-PWR, medium-heat CSNF WPs at the center of the repository (l4c3 location in Table 2-2)

Curves are plotted for the July 1997 TSPA-VA preliminary base-case I x 1 parameter set and the December 1997 TSPA-VA base-case I x 1 $\alpha_{f,mean}$ parameter set. For the I x 1 case, the infiltration flux at location l4c3 is 10.9 mm/yr. The symbol I stands for the nominal infiltration-flux q_{inf} map (average q_{inf} = 7.8 mm/yr) for the present-day climate. The variable α_f is the van Genuchten "alpha" parameter for fractures. The variable q_{liq} stands for liquid-phase flux 3 m above the drift.

Differences in the liquid-phase flux q_{liq} 3 m above the drift (Figure 3-3e) between the July 1997 preliminary base-case and December 1997 base-case parameter sets probably result from the differences in the respective values of FMX. The larger FMX in the preliminary (July 1997) base-case set results in less effective condensate shedding, which causes more condensate buildup above the drift. The greater condensate buildup results in a less stable boiling/condensate front, which results in a fluctuating q_{liq} history between 60 yr and 600 yr.

The magnitude of infiltration flux stingily affects rock dryout and *RH* reduction (compare Figure 3-2a, Figure 3-2b, and Figure 3-2c). **Figure 3-4**c and Figure 3-4d also show the strong dependence of rock dryout and *RH* reduction on the magnitude of infiltration flux. The dependence of near-field temperature increase on infiltration flux is much weaker (Figure 3-4a and 3-4b). A factor of nine difference in infiltration flux causes less than a 10°C difference in temperature.

Figure 3-4 Summary of TH conditions are plotted for "average" 21-PWR, medium-heat CSNF WPs at the center of the repository (l4c3 location in Table 2-2)

Curves are plotted for the following parameter sets and infiltration assumptions: December 1997 TSPA-VA base-case I x 1 $\alpha_{f,mean}$, December 1997 TSPA-VA base-case I x 0.33 $\alpha_{f,min}$, December 1997 TSPA-VA base-case I x 3 $\alpha_{f,min}$, December 1997 TSPA-VA base-case I x 0.33 $\alpha_{f,max}$, and December 1997 TSPA-VA base-case I x 3 $\alpha_{f,max}$.

The symbol I stands for the nominal infiltration-flux q_{inf} map (average q_{inf} = 7.8 mm/yr) for the present-day climate. The variable α_f is the van Genuchten "alpha" parameter for fractures. The variable q_{liq} stands for liquid-phase flux 3 m above the drift.

The extent of rock dryout and *RH* reduction is relatively weakly dependent on the value of α_f (Figure 3-4c and Figure 3-4d). Temperature increase is also weakly dependent on the value of α_f (Figure 3-4a and Figure 3-4b).

With the exception of the I x 0.33 $\alpha_{f,max}$ case, the peak value of q_{liq} is not strongly dependent on infiltration flux (Figure 3-4e). The lower value of q_{liq} for the I x 0.33 $\alpha_{f,max}$ case, compared to the I x 0.33 $\alpha_{f,min}$ case, results from its smaller value of FMX, which facilitates more effective condensate shedding.

For TSPA-VA (CRWMS M&O, 1998), TH conditions on WPs are binned according to the time for WPs to attain $RH = 85\%$, which is called $t(RH = 85\%)$. An RH of 85% was selected because it is assumed in TSPA-VA to be the critical RH for the initiation of atmospheric corrosion. A useful way to display the distribution of TH conditions on all WPs in the repository is to use a CCDF of $t(RH = 85\%)$.

Figure 3-5a shows the influence of the differences between the July 1997 TSPA-VA preliminary base-case parameter set and the December 1997 TSPA-VA base-case set on the CCDF of $t(RH = 85\%)$. The stronger fracture wicking in the July 1997 preliminary base-case set reduces $t(RH = 85\%)$, particularly for medium-to-large values of $t(RH = 85\%)$.

Figure 3-5. CCDF of the time required for WPs to rewet to a relative humidity *RH* of 85% for the point-load design with no backfill and the nominal infiltration-flux q_{inf} map for the present-day climate

Curves are plotted in (a) for the July 1997 TSPA-VA preliminary base-case I x 1 and the December 1997 TSPA-VA base-case I x 1 $\alpha_{f,mean}$ parameter sets and in (b) for the December 1997 TSPA-VA base-case I x 1 $\alpha_{f,mean}$, the November 1997 TH, and December 1997 modified-TH parameter sets, where the symbol I stands for the nominal infiltration-flux q_{inf} map (average q_{inf} = 7.8 mm/yr) for the present-day climate.

The magnitude of percolation flux significantly affects the magnitude of $t(RH = 85\%)$, but it does not affect the overall shape of the CCDF of $t(RH = 85\%)$ (**Figure 3-6**). Relative to the I x 1 $\alpha_{f,mean}$ case, a threefold decrease in percolation flux results in a 40% increase in $t(RH = 85\%)$ for the median WP, while a threefold increase in percolation flux results in a 40% decrease in $t(RH = 85\%)$ for the median WP. The influence of the range of α_f that was considered is not as strong as a threefold difference in percolation flux. For the I x 0.33 cases, the $t(RH = 85\%)$ for the median WP is 6% greater for the $\alpha_{f,min}$ case than it is for the $\alpha_{f,max}$ case; for the I x 3 cases, the $t(RH = 85\%)$ for the median WP is 15% greater for the $\alpha_{f,min}$ case than it is for the $\alpha_{f,max}$ case.

Figure 3-6. CCDF of the time required for WPs to rewet to a relative humidity *RH* of 85% for the point-load design with no backfill for the December 1997 TSPA-VA base-case hydrologic property sets

Curves are plotted, from left to right, for five December 1997 TSPA-VA base-case hydrologic property sets: (1) I x 3, $\alpha_{f,min}$, (2) I x 3 $\alpha_{f,max}$, (3) I x 1 $\alpha_{f,mean}$, (4) 0.33 x I $\alpha_{f,max}$, and (5) 0.33 x I $\alpha_{f,min}$, where α_f is the van Genuchten "alpha" parameter for fractures.

The subscripts min, mean, and max stand for the minimum, mean, and maximum values of α_f and the symbol I stands for the nominal infiltration-flux q_{inf} map (average q_{inf} = 7.8 mm/yr) for the present-day climate.

3.2 Influence of Matrix Properties on EBS TH Conditions

In attempting to model the SHT and the Large-Block Test (LBT) with the hydrologic property values for the tsw36 unit from the July 1997 TSPA-VA preliminary base-case (and December 1997 TSPA-VA base-case) parameter set, it was found that capillary forces associated with these property values were far too strong, contrary to experimental data, to

allow the formation of a superheated dryout zone (Buscheck, 1997; Hardin et al., 1998). This difficulty was attributed to large values of D_{imb} in that unit, which led to rapid rewetting of the rock, thereby preventing any rock dryout and temperature increase

This difficulty was addressed in November 1997 by the development of a TH parameter set (Table 2-11 and Table 2-12) calibrated by Lawrence Livermore National Laboratory (LLNL) and Lawrence Berkeley National Laboratory (LBNL) with temperature measurements from the SHT ("T-H Modeling of the Single-Heater Test with Site-Scale Calibrated Properties," LBNL memorandum to G. S. Bodvarsson, LLNL, from J. Birkholzer, November 19, 1997; Buscheck, 1997 #635]. Analysis of the SHT (Hardin et al., 1998) shows that the value of D_{imb} for the tsw36 in the July 1997 TSPA-VA preliminary base-case parameter set is too large to allow rock dryout and temperature increase in the nominally superheated zone. The value of D_{imb} in the tsw36 unit in the November 1997 TH set is reduced by a factor of 12 relative to the July 1997 preliminary base-case set. The reduced value produces more rock dryout in this unit and a closer match to temperatures observed in the SHT. The November 1997 TH set also has larger values of α_f, and thus less capillary-driven rewetting flux in the fractures, than does the July 1997 preliminary base-case set (Table 3-2). The values of a_f in the November 1997 TH set are similar to those of the December 1997 TSPA-VA base-case set.

The difficulty with the large values of D_{imb} was addressed at LLNL in December 1997 by developing a TH parameter set that is a modification of the November 1997 TH parameter set. Table 2-13 contains the matrix parameters in the tsw36 and tsw37 units for this December 1997 modified-TH parameter set. Fracture properties, and matrix properties for other units, were not changed from values in the November 1997 TH parameter set. The modifications were made to that set so that the value of D_{imb} for the tsw36 and tsw37 units would be the same as those in the tsw34 unit. These changes were made because laboratory measurements from Flint et al. (1996b) indicate that the values of D_{imb} for the tsw36 and tsw37 units are no greater than those for the tsw34 unit. The principal change was a reduction, by a factor of 28, in the value of D_{imb} for the basal vitrophyre (tsw37). The value for the tsw36 unit was reduced by a factor of 2.8.

The influence of matrix imbibition in the tsw36 unit, for the December 1997 TSPA-VA base-case set, is apparent in **Figure 3-7**a and Figure 3-7d. On the western side of the repository, which lies within the tsw36 unit (Figure 3-1a), matrix imbibition greatly thwarts rock dryout and *RH* reduction in the near field and on WPs.

Figure 3-7. **Relative humidity *RH* on the surface of "average" 21-PWR, medium-heat CSNF WPs plotted for the December 1997 TSPA-VA base-case I x 1 $\alpha_{f,mean}$ parameter set at (a) 500 yr and (d) 1000 yr, for the November 1997 TH parameter set at (b) 500 yr and (e) 1000 yr, and for the December 1997 modified-TH parameter set at (c) 500 yr and (f) 1000 yr**

The symbol I stands for the nominal infiltration-flux q_{inf} map (average q_{inf} = 7.8 mm/yr) for the present-day climate. The variable α_f is the van Genuchten "alpha" parameter for fractures.

Reducing D_{imb} for the tsw36 unit in the November 1997 TH parameter set increases rock dryout and *RH* reduction in the near field and on WPs, especially on the western side of the repository (compare Figure 3-7a and Figure 3-7b; also compare Figure 3-7d with Figure 3-7e).

For the December 1997 modified-TH parameter set, the changes to D_{imb} in the tsw36 and tsw37 units resulted in more rock dryout in those units (Hardin et al., 1998). However, the changes produced only a small additional reduction (compared to the November 1997 TH set) in *RH* in the near field and on WPs; this was primarily in the southwestern region of the repository (compare Figure 3-7b and Figure 3-7c; also compare Figure 3-7e with Figure 3-7f).

Figure 3-8 summarizes the differences in the near field and on WPs for these three parameter sets at the repository center (the l4c3 location in Table 2-2). Because the tsw36 and tsw37 are so far removed (vertically) from the repository horizon at this location, changes to the value of D_{imb} in the tsw36 and tsw37 have a relatively small effect on *RH* in the near field and on WPs (Figure 3-8c and Figure 3-8d). The differences in D_{imb} have an even smaller effect on temperature (Figure 3-8a and Figure 3-8b). The differences in D_{imb} also have a relatively small effect on q_{liq} 3 m above the drift (Figure 3-8e).

Figure 3-8. Summary of TH conditions are plotted for "average" 21-PWR, medium-heat CSNF WPs at the center of the repository (l4c3 location in Table 2-2)

Curves are plotted for the following parameter sets and infiltration assumptions: December 1997 TSPA-VA base-case I x 1 $\alpha_{f,mean}$, November 1997 TH parameter set, and December 1997 modified-TH parameter set. For the I x 1 case, the infiltration flux at location l4c3 is 10.9 mm/yr. The symbol I stands for the nominal infiltration-flux q_{inf} map (average q_{inf} = 7.8 mm/yr) for the present-day climate. The variable α_f is the van Genuchten "alpha" parameter for fractures. The variable q_{liq} stands for liquid-phase flux 3 m above the drift.

Figure 3-5b indicates that D_{imb} influences the CCDF of $t(RH = 85\%)$ for the early- and late-time portions of the CCDF curve; D_{imb} has a smaller effect for the intermediate-time portion of the CCDF of $t(RH = 85\%)$. The early-time portion of the CCDF of $t(RH = 85\%)$ is primarily influenced by WPs located at the repository edges. Because much of the western edge of the repository lies in the tsw36, changes to D_{imb} in the tsw36 (and in tsw37) will be evident in the early-time portion of the CCDF of $t(RH = 85\%)$. Because the intermediate-time portion of the CCDF of $t(RH = 85\%)$ is primarily influenced by the magnitude of percolation flux rather than by the magnitude of matrix imbibition flux, the value of D_{imb} will be less influential in that portion of the CCDF. The late-time portion of the CCDF pertains to regions of the repository with relatively low percolation flux. In the low-percolation-flux regions, rewetting is primarily influenced by matrix imbibition flux rather than by percolation flux. The low-percolation-flux regions of the repository for which rock dryout extends into the tsw36 and tsw37 units will be influenced by the value of D_{imb} in those units. Consequently, the late-time portion of the CCDF of $t(RH = 85\%)$ is influenced by the value of D_{imb} in the tsw36 and tsw37.

3.3 Comparison of Predicted TH Behavior Between the LLNL Multiscale TH Modeling Approach and the LBNL East–West Cross-Sectional TH Model

In this section, a comparison is made between EBS TH conditions predicted by the multiscale TH modeling approach used in this study and an east–west cross-sectional TH model developed at LBNL (Haukwa et al., 1998). Because the east–west model does not predict in-drift TH conditions, and because RH and liquid-phase saturation data were not provided from that model, the comparison is restricted to predictions of host-rock temperatures by the respective modeling approaches (**Figure 3-9**).

Figure 3-9. Comparison of predicted temperatures at (a) center of the repository (l4c3 location in Table 2-2) and (b) 100 m from the edge of the repository (l4c1 location) for the December 1997 TSPA-VA base-case I x 1 $\alpha_{f,mean}$ parameter set

The symbol I stands for the nominal infiltration-flux q_{inf} map (average q_{inf} = 7.8 mm/yr) for the present-day climate, and the variable α_f is the van Genuchten "alpha" parameter for fractures.

The LLNL multiscale, TH modeling methodology is used to predict drift-wall temperature adjacent to an "average" 21-PWR, medium-heat CSNF WP. The LBNL E–W cross-sectional TH model is used to predict the drift temperature, which is averaged over the cross section of the drift, arising from a line-averaged heat-source representation of WP decay heat.

Before discussing the differences in the temperatures predicted by the two approaches (Figure 3-9) it is important to discuss the differences in the models. The temperature predicted by the LLNL multiscale model is the perimeter-averaged, drift-wall temperature adjacent to an "average" 21-PWR, medium-heat CSNF WP. The multiscale modeling approach discretely represents the decay-heat source from individual WPs. Thus, some of the drift-wall locations are hotter than shown in Figure 3-9, and some are considerably cooler. The drift-wall grid blocks, over which the temperature is averaged, extend 0.5 m into the host rock surrounding the drift. The temperature prediction in the LBNL east–west model is for a grid block that occupies the entire cross section of the drift; it is a lumped representation of the drift temperature. Moreover, because the LBNL east–west model uses a line-averaged heat source, it axially smears out the differences between hot-WP locations and cold-WP locations along the drift.

It is also important to note that the lateral grid-block spacing in the two approaches is quite different. From the drift centerline to the pillar centerline, the lateral grid-block spacing in the LLNL multiscale model is 0.7225 m, 1.5375 m, 0.5 m (at the drift wall), 1.0 m, 1.5 m, 2.24 m, 3.0 m, and 3.5 m. In the LBNL east–west model, the lateral grid-block spacing is 2.5 m and 12.5 m. Cross-sectional area of the emplacement is 25 m^2 in the LBNL east–west model; it is 20.43 m^2 (which corresponds to the actual cross-sectional area for a drift diameter of 5.1 m) in the LLNL multiscale model. Therefore, the lumped drift temperature in the LBNL east–west model extends over a cross section that is about 22% larger than the actual cross section of the drift.

Another difference between the modeling approaches concerns the mountains-scale dimensionality. The LLNL multiscale model represents 3-D mountain-scale heat flow, which assumes the actual areal extent of the heated footprint; the LBNL east–west model is a cross-sectional model with a reflected boundary at the east–west midpoint of the repository. Thus, the LBNL model assumes that the overburden thickness of the entire repository area can be approximated with the overburden thickness distribution along the middle row of dots (Figure 2-1c) between the western repository boundary and the midpoint of the repository. Because the eastern half of the repository has much less overburden thickness than the western half (Figure 2-1a), this east–west symmetry approximation overrepresents the effective overburden thickness for the eastern half of the repository. The cross-sectional geometry of the LBNL east–west model implicitly assumes that mountain-scale heat loss in the north–south dimension is negligible, which is a reasonable assumption given the large north–south dimension of the repository.

Another difference between the two modeling approaches concerns the areal power density (APD) assumed in the models. The initial APD in the LLNL multiscale model is 92.3 kW/acre; it is 99.4 kW/acre in the LBNL east–west model. Thus, the LBNL model has a 7.7% larger APD than does the LLNL model. The lower APD in the LLNL multiscale model was used to approximate the influence of the 4 empty drifts (out of a total of 104 drifts) and the influence of the cold-trap mechanism that will cause vapor and latent heat to be transported beyond the last WP in each drift (Hardin et al., 1998). The bulkheads at the ends of each drift are about 30 m beyond the outer WP. It was assumed that the effective footprint of heating would extend about 18 m beyond the last WP along the eastern and western boundaries of the repository. Overall, the empty drifts and the extended heated footprint cause a 7.7% reduction in the overall AML and in the APD.

At the center of the repository (the l4c3 location in Table 2-2), the two modeling approaches predict an almost identical duration of boiling (Figure 3-9a). At the edge repository location, which is 100 m from the western edge of the repository in the multiscale model (the l4c1 location in Table 2-2), the LBNL east–west model predicts a longer duration of boiling than does the LLNL multiscale model. One reason for this difference is that the LBNL model representation of the heated repository footprint extends slightly further to the west than it does in the LLNL model. This difference is seen when comparing the shaded area and the rectangular area in Figure 2-1c for the middle row of dots. The shaded area at the middle row of dots in Figure 2-1c corresponds to the lateral extent of decay heat in the LBNL model. Thus, the l4c1 location in the LBNL model is somewhat further from the western repository edge than it is in the LLNL model.

During the post-boiling period, the temperatures predicted by the two modeling approaches are in good agreement. During the early-time heat-up period, the coarse lateral and axial grid-block spacing in the LBNL east–west model does not capture the rapid drift-wall temperature increase that the more finely gridded LLNL multiscale model predicts. Because of the coarse lateral grid-block spacing in the LBNL east–west model, the model smears out the lateral temperature gradient between the drift and the mid-pillar location. Thus, the model tends to overpredict the temperature at the mid-pillar location and thereby prevent condensate from shedding between drifts. The fine lateral grid-block spacing in the LLNL multiscale model captures the influence that the lateral temperature gradient has on allowing condensate to shed between drifts. The tendency for the LBNL east-west model to underepresent condensate shedding results in a more substantial condensate buildup above the repository horizon. Also, the line-averaged, heat-source approximation smears out differences in temperature between otherwise hot- and cold-WP locations. The lack of distinction between the hot and cold locations prevents condensate from breaking through cold-WP locations along the drift. Altogether, the underprediction of condensate shedding between drifts and condensate breakthrough at cold-WP locations causes the LBNL east–west model to build up more condensate above the repository horizon, which leads to unstable heat-pipe behavior. This unstable behavior is exhibited by the rapid decline from superheated conditions to heat-pipe conditions (Figure 3-9a) and the rapid increase, once again, to superheated conditions at about 400 yr. Notice that, during the second superheated period predicted by the LBNL east–west model, the temperature climbs to be almost exactly that predicted by the LLNL multiscale model.

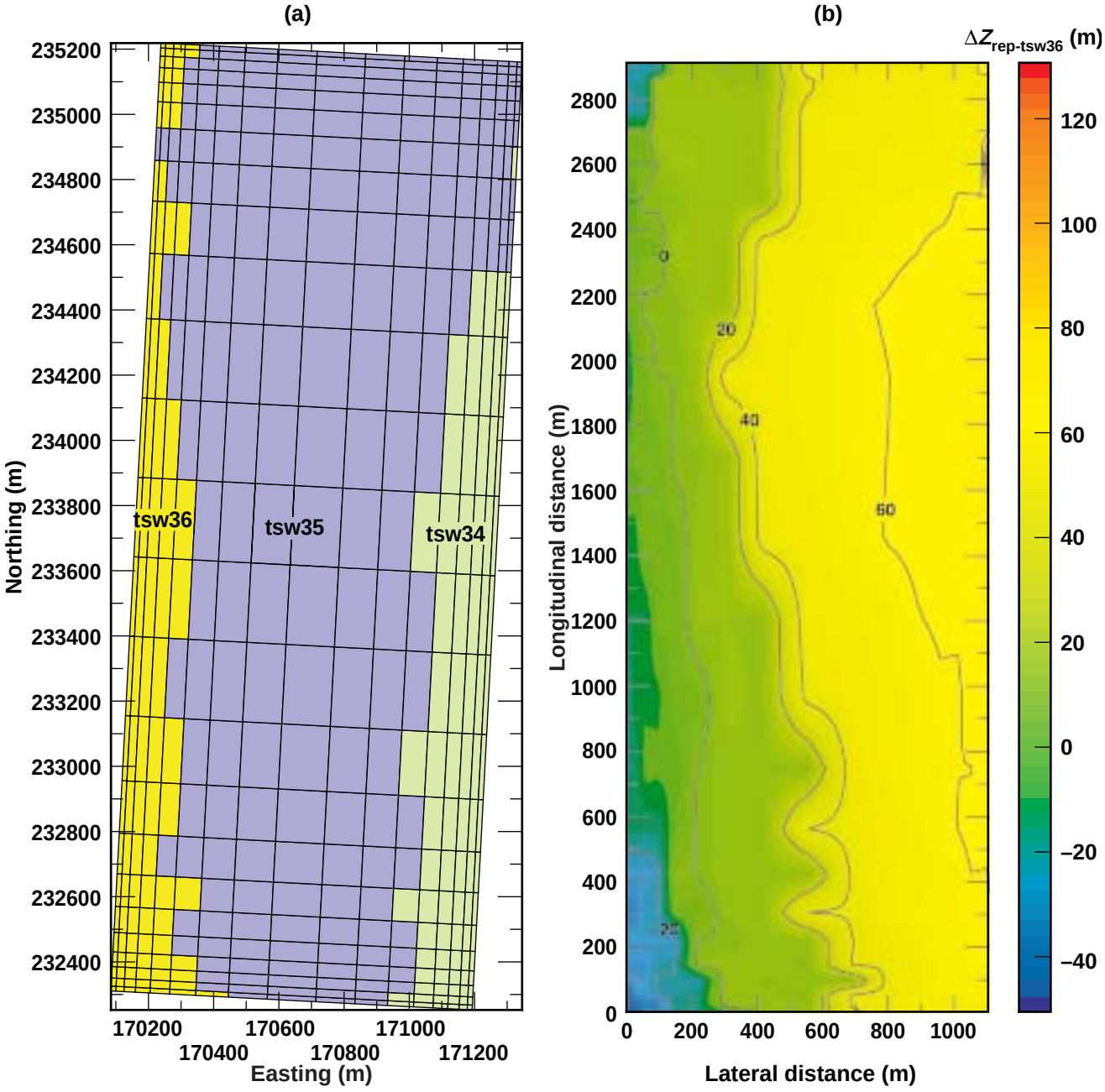

Figure 3-1 Plan view of host-rock distribution (a) shown for the SMT-model grid of the repository area as a function of Nevada-State coordinates (b) contour map of the vertical distance $\Delta Z_{rep\text{-}tsw36}$ between the repository horizon and the top of the tsw36 hydrogeologic model unit shown as a function of distance from the southwest corner of the repository area in the SMT model, where the SMT model is the smeared-heat-source mountain-scale thermal model

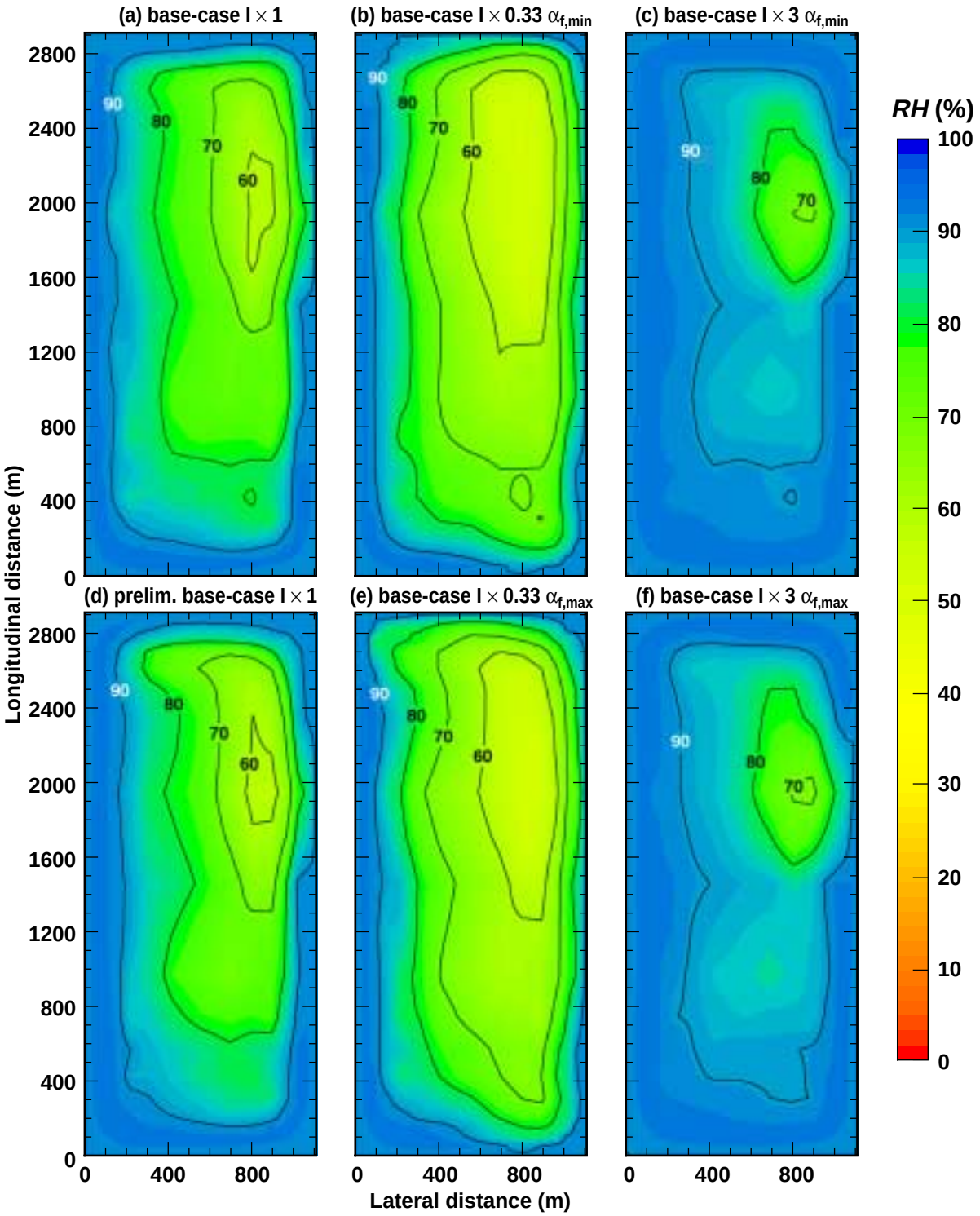

Figure 3-2. Relative humidity RH on the surface of "average" 21-PWR, medium-heat CSNF WPs at 1000 yr for the point-load design with no backfill. Curves are plotted for the following parameter sets and infiltration assumptions: (a) December 1997 TSPA-VA base-case I × 1 $\alpha_{f,mean}$, (b) December 1997 TSPA-VA base-case I × 0.33 $\alpha_{f,min}$, (c) December 1997 TSPA-VA base-case I × 3 $\alpha_{f,min}$, (d) July 1997 TSPA-VA preliminary base-case I × 1, (e) December 1997 TSPA-VA base-case I × 0.33 $\alpha_{f,max}$, and (f) December 1997 TSPA-VA base-case I × 3 $\alpha_{f,max}$. The symbol I stands for the nominal infiltration-flux q_{inf} map (average q_{inf} = 7.8 mm/yr) for the present-day climate, and α_f is the van Genuchten alpha parameter for fractures.

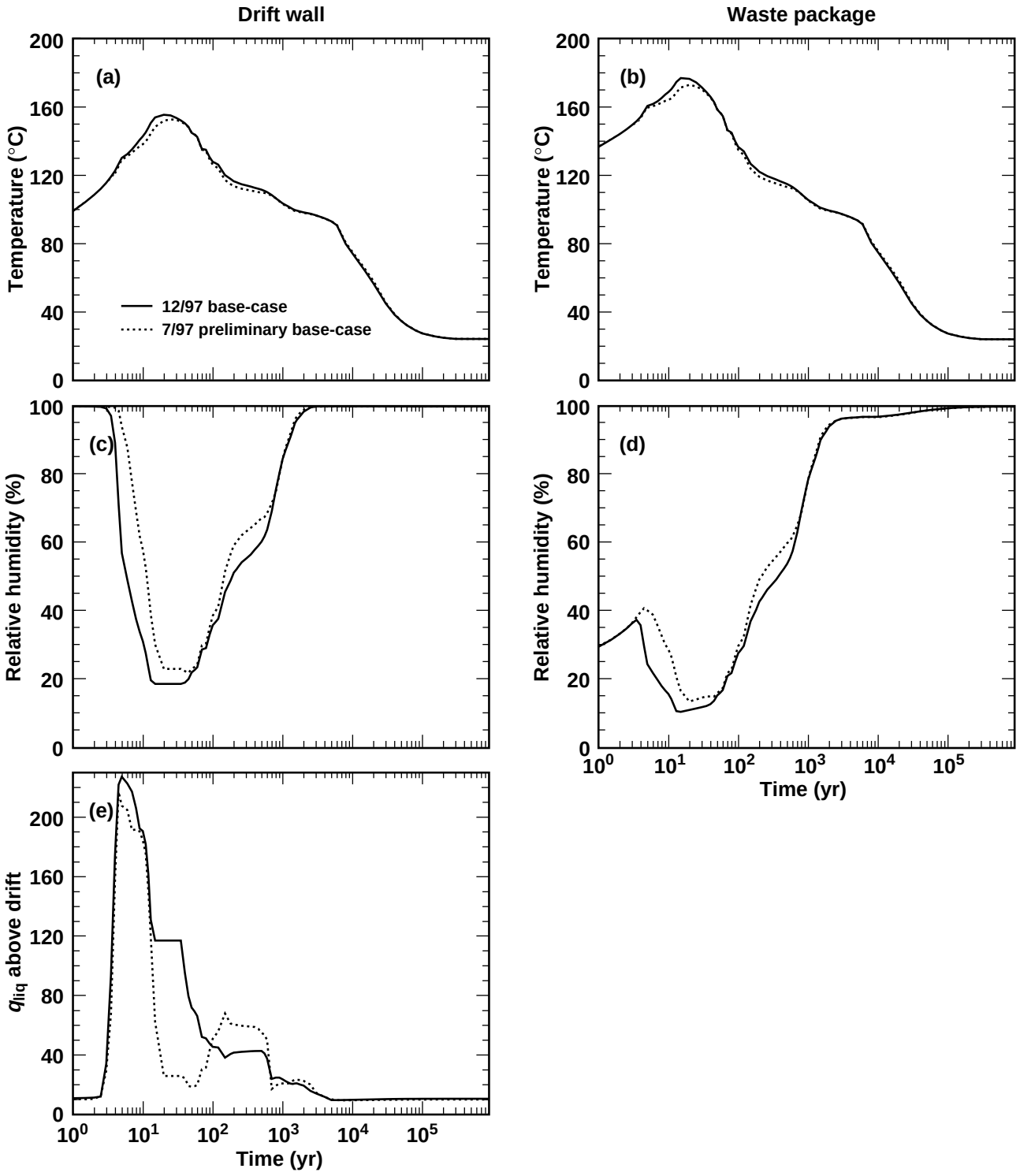

Figure 3-3. Summary of TH conditions are plotted for "average" 21-PWR, medium-heat CSNF WPs at the center of the repository (l4c3 location in Table 2-2). Curves are plotted for the July 1997 TSPA-VA preliminary base-case I × 1 parameter set and the December 1997 TSPA-VA base-case I × 1 $\alpha_{f,mean}$ parameter set. For the I × 1 case, the infiltration flux at location l4c3 is 10.9 mm/yr. The symbol I stands for the nominal infiltration-flux q_{inf} map (average q_{inf} = 7.8 mm/yr) for the present-day climate. The variable α_f is the van Genuchten "alpha" parameter for fractures. The variable q_{liq} stands for liquid-phase flux 3 m above the drift.

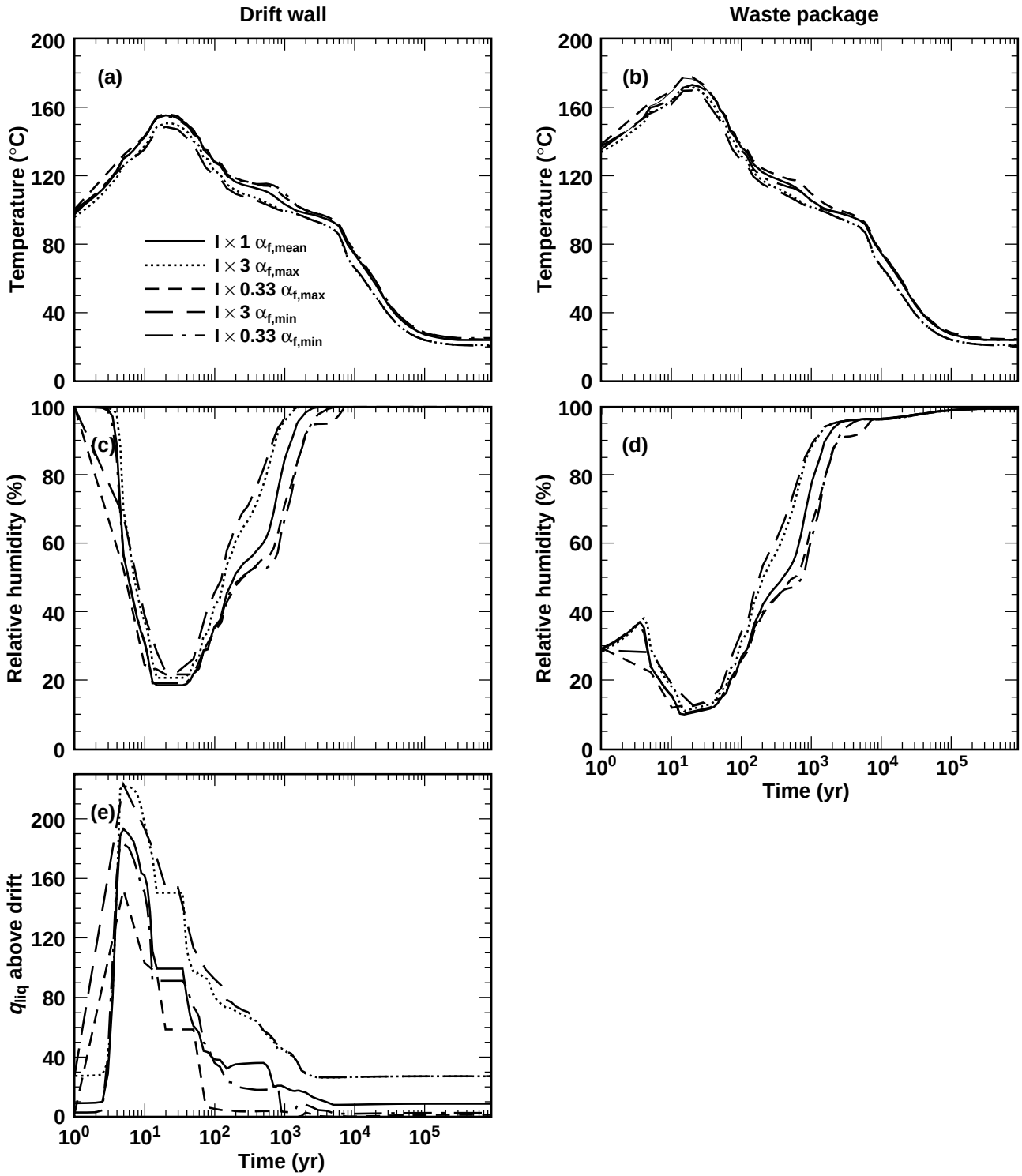

Figure 3-4 Summary of TH conditions are plotted for "average" 21-PWR, medium-heat CSNF WPs at the center of the repository (l4c3 location in Table 2-2) Curves are plotted for the following parameter sets and infiltration assumptions: December 1997 TSPA-VA base-case I × 1 $\alpha_{f,mean}$, December 1997 TSPA-VA base-case I × 0.33 $\alpha_{f,min}$, December 1997 TSPA-VA base-case I × 3 $\alpha_{f,min}$, December 1997 TSPA-VA base-case I × 0.33 $\alpha_{f,max}$, and December 1997 TSPA-VA base-case I × 3 $\alpha_{f,max}$.The symbol I stands for the nominal infiltration-flux q_{inf} map (average q_{inf} = 7.8 mm/yr) for the present-day climate. The variable α_f is the van Genuchten "alpha" parameter for fractures. The variable q_{liq} stands for liquid-phase flux 3 m above the drift.

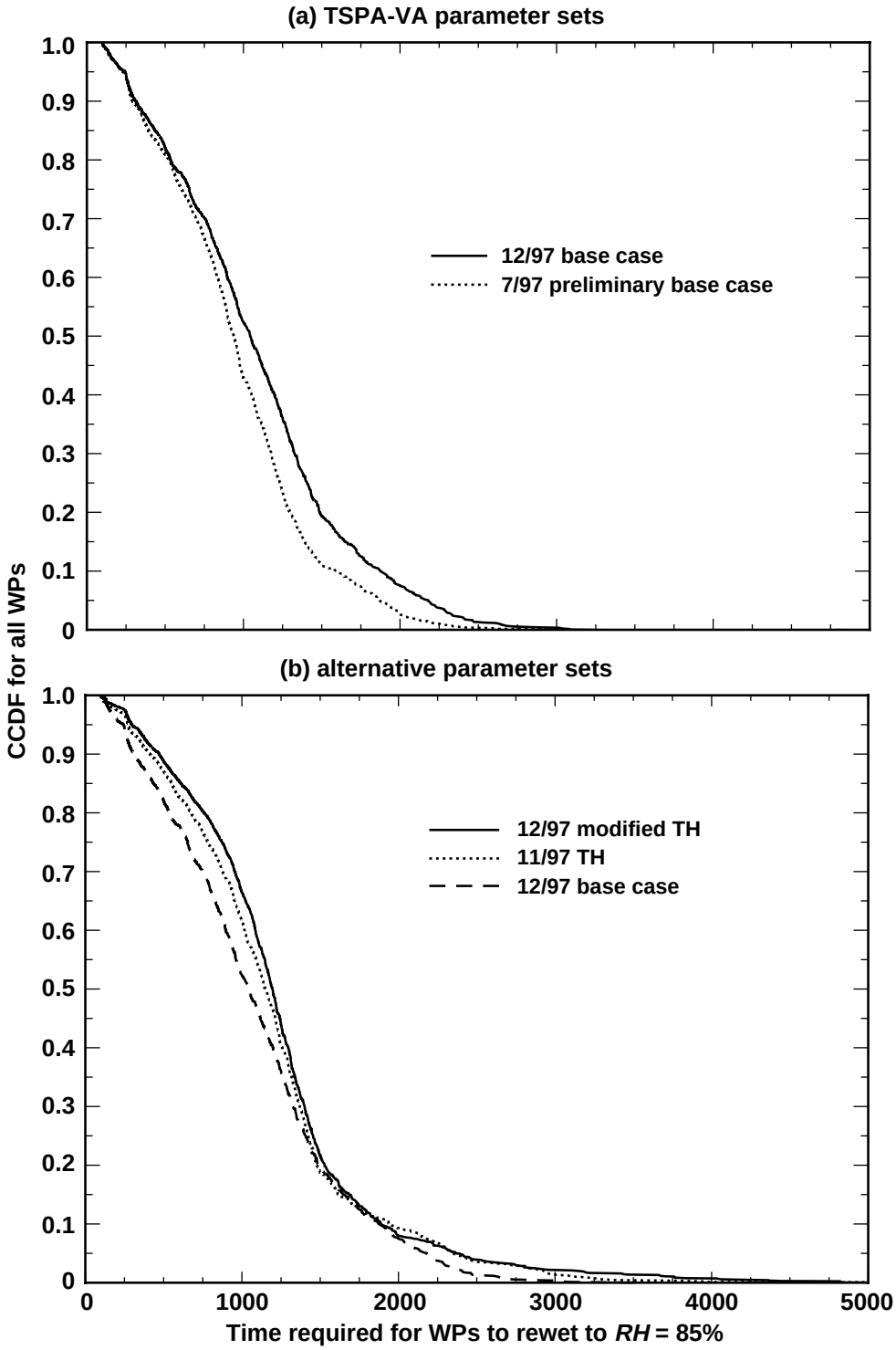

Figure 3-5. CCDF of the time required for WPs to rewet to a relative humidity RH of 85% for the point-load design with no backfill and the nominal infiltration-flux q_{inf} map for the present-day climate. Curves are plotted in (a) for the July 1997 TSPA-VA preliminary base-case I × 1 and the December 1997 TSPA-VA base-case I × 1 $\alpha_{f,mean}$ parameter sets and in (b) for the December 1997 TSPA-VA base-case I× 1 $\alpha_{f,mean}$, the November 1997 TH, and December 1997 modified-TH parameter sets, where the symbol I stands for the nominal infiltration-flux q_{inf} map (average q_{inf} = 7.8 mm/yr) for the present-day climate.

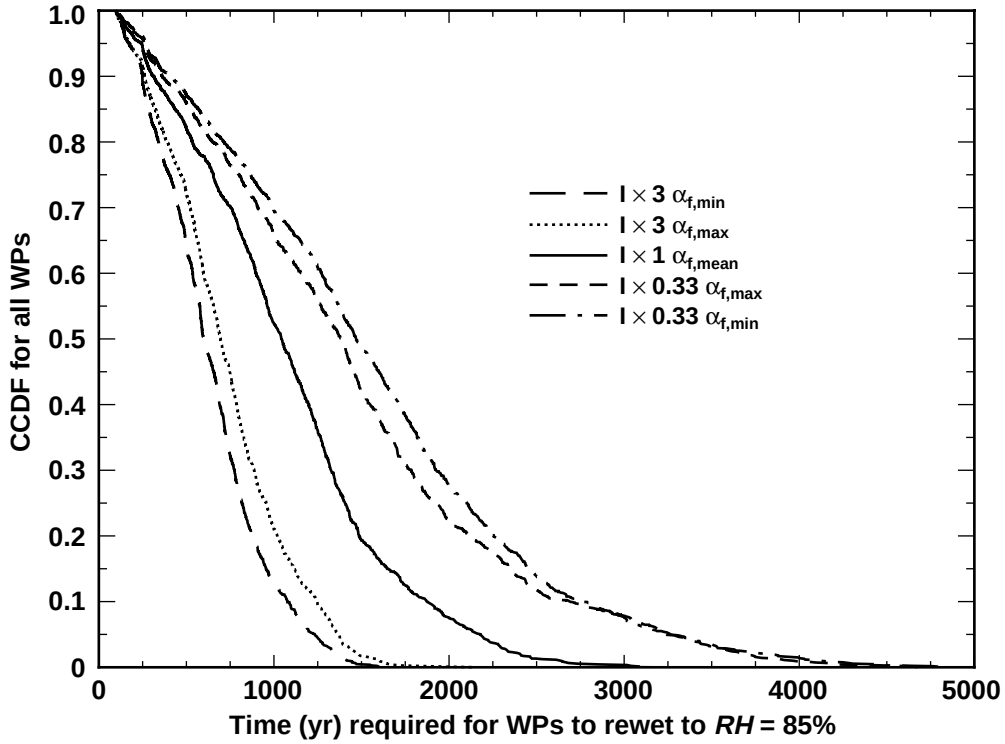

Figure 3-6. CCDF of the time required for WPs to rewet to a relative humidity RH of 85% for the point-load design with no backfill for the December 1997 TSPA-VA base-case hydrologic property sets. Curves are plotted, from left to right, for five December 1997 TSPA-VA base-case hydrologic property sets: (1) $I \times 3$, $\alpha_{f,min}$, (2) $I \times 3$ $\alpha_{f,max}$, (3) $I \times 1$ $\alpha_{f,mean}$, (4) $0.33 \times I$ $\alpha_{f,max}$, and (5) $0.33 \times I$ $\alpha_{f,min}$, where α_f is the van Genuchten "alpha" parameter for fractures. The subscripts min, mean, and max stand for the minimum, mean, and maximum values of α_f and the symbol I stands for the nominal infiltration-flux q_{inf} map (average q_{inf} = 7.8 mm/yr) for the present-day climate.

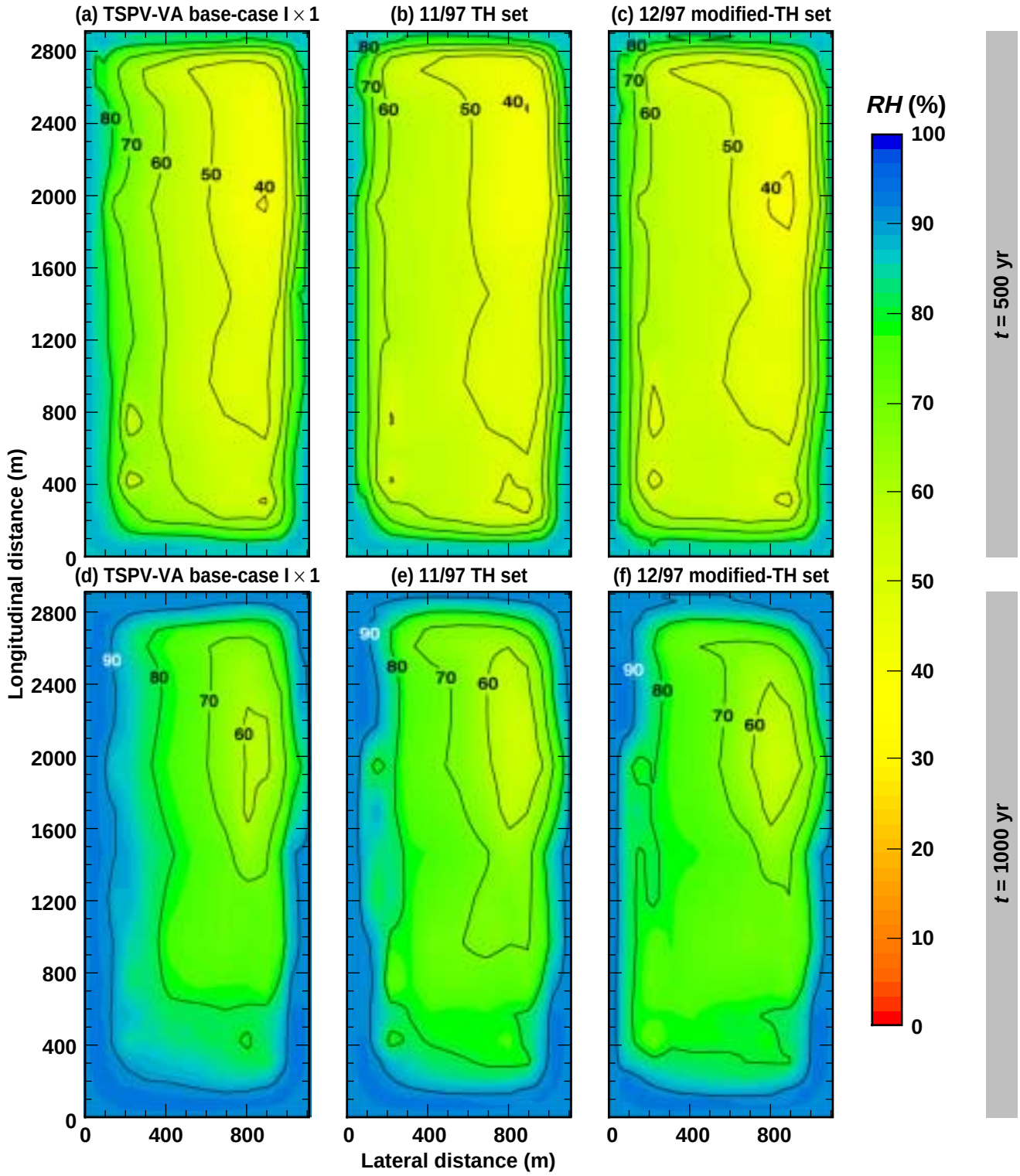

Figure 3-7. Relative humidity RH on the surface of "average" 21-PWR, medium-heat CSNF WPs plotted for the December 1997 TSPA-VA base-case I × 1 $\alpha_{f,mean}$ parameter set at (a) 500 yr and (d) 1000 yr, for the November 1997 TH parameter set at (b) 500 yr and (e) 1000 yr, and for the December 1997 modified-TH parameter set at (c) 500 yr and (f) 1000 yr. The symbol I stands for the nominal infiltration-flux q_{inf} map (average q_{inf} = 7.8 mm/yr) for the present-day climate. The variable α_f is the van Genuchten "alpha" parameter for fractures.

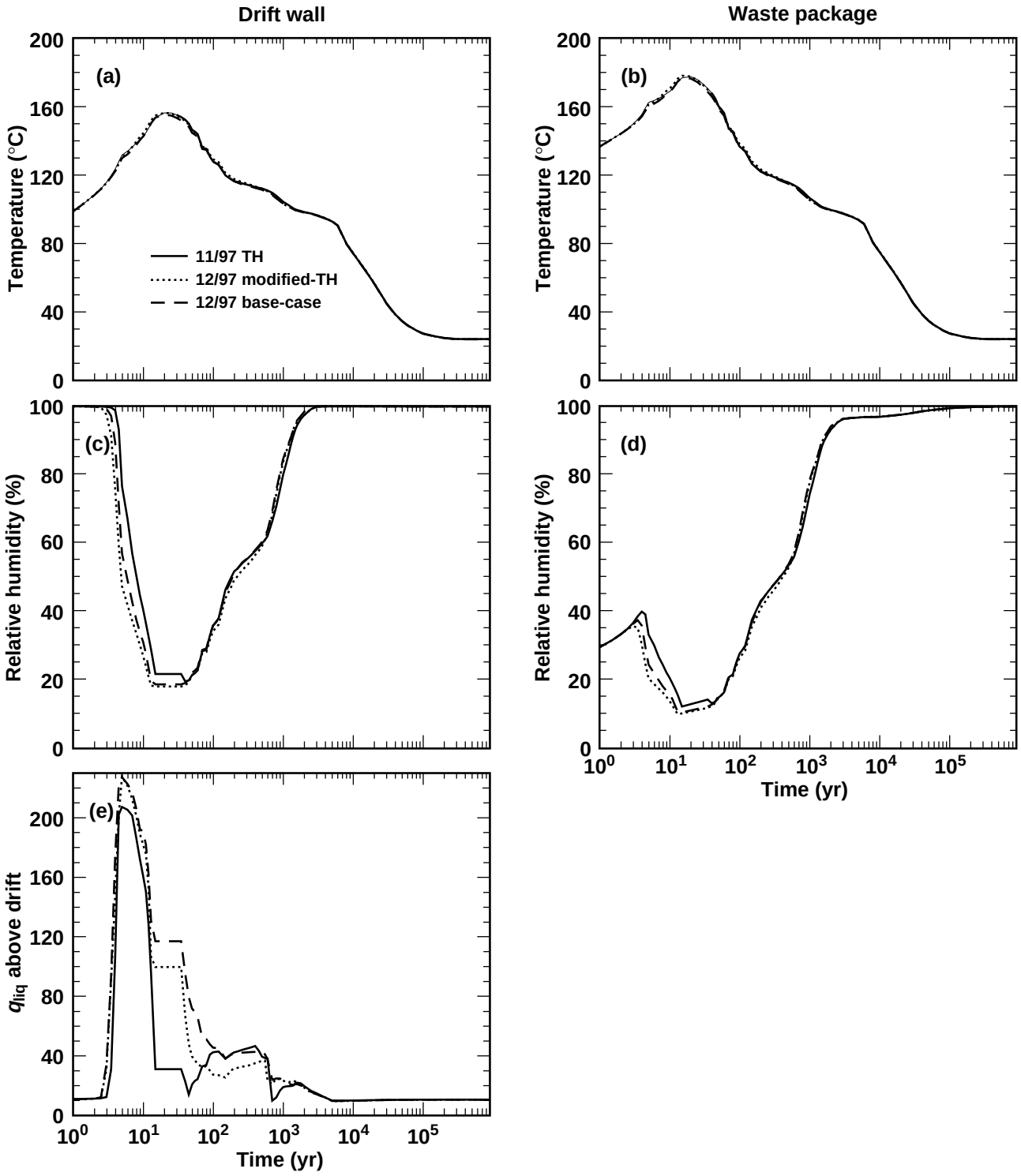

Figure 3-8. Summary of TH conditions are plotted for "average" 21-PWR, medium-heat CSNF WPs at the center of the repository (l4c3 location in Table 2-2). Curves are plotted for the following parameter sets and infiltration assumptions: December 1997 TSPA-VA base-case $I \times 1$ $\alpha_{f,mean}$, November 1997 TH parameter set, and December 1997 modified-TH parameter set. For the $I \times 1$ case, the infiltration flux at location l4c3 is 10.9 mm/yr. The symbol I stands for the nominal infiltration-flux q_{inf} map (average q_{inf} = 7.8 mm/yr) for the present-day climate. The variable α_f is the van Genuchten "alpha" parameter for fractures. The variable q_{liq} stands for liquid-phase flux 3 m above the drift.

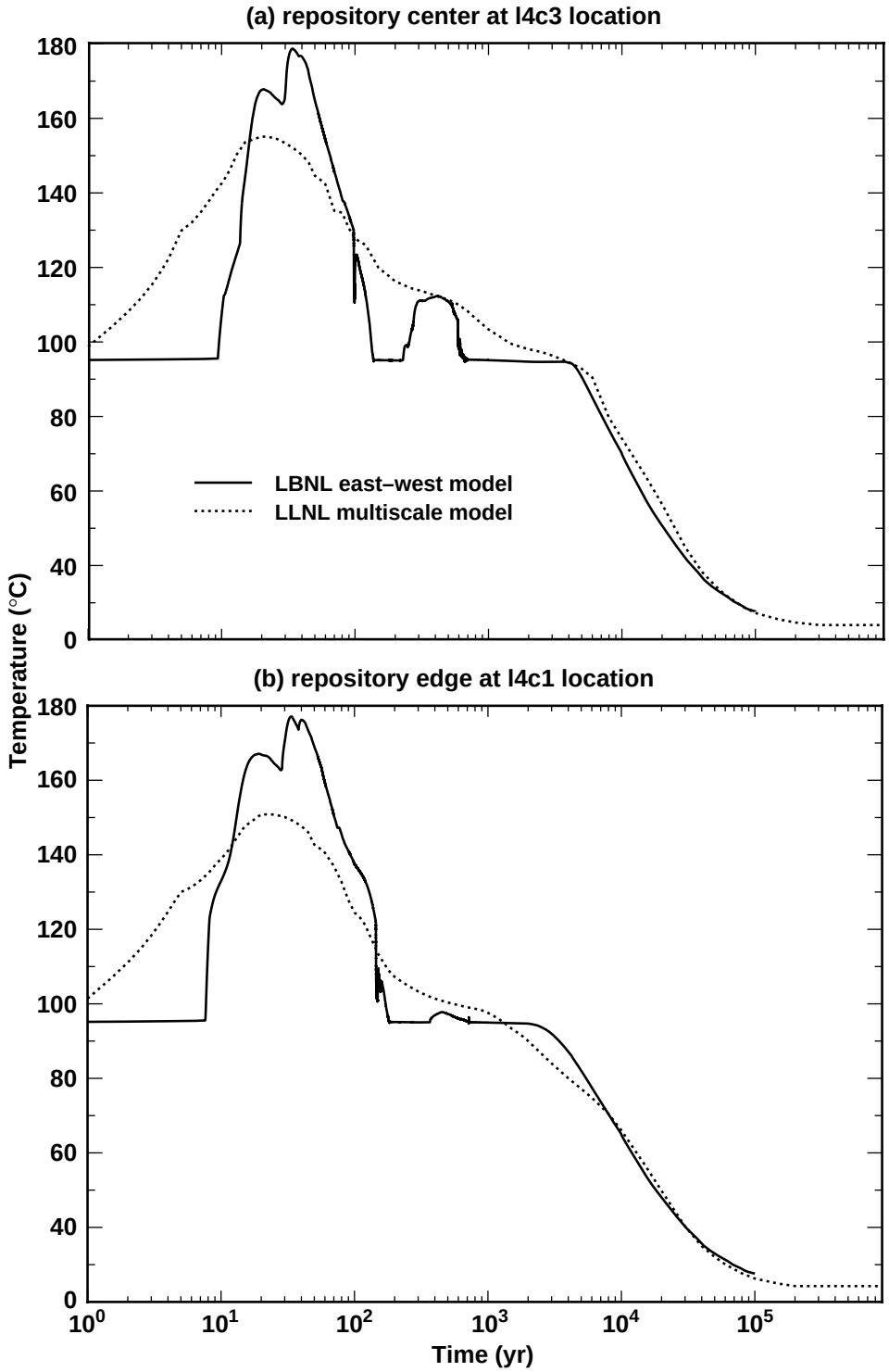

Figure 3-9. Comparison of predicted temperatures at (a) center of the repository (l4c3 location in Table 2-2) and (b) 100 m from the edge of the repository (l4c1 location) for the December 1997 TSPA-VA base-case I × 1 $\alpha_{f,mean}$ parameter set. The symbol I stands for the nominal infiltration-flux q_{inf} map (average q_{inf} = 7.8 mm/yr) for the present-day climate, and the variable α_f is the van Genuchten "alpha" parameter for fractures. The LLNL multiscale, TH modeling methodology is used to predict drift-wall temperature adjacent to an "average"21-PWR, medium-heat CSNF WP. The LBNL E–W cross-sectional TH model is used to predict the drift temperature, which is averaged over the cross section of the drift, arising from a line-averaged heat-source representation of WP decay heat.

4. Conclusions

The multiscale thermohydrologic (TH) modeling approach, which integrates the results from one-dimensional (1-D), two-dimensional (2-D), and three-dimensional (3-D) drift-scale models and a 3-D mountain-scale model, is used to analyze the sensitivity of near-field and the engineered-barrier-system (EBS) TH variables to alternative hydrologic property sets and infiltration-flux assumptions. The EBS TH variables predicted by this approach are required by Total System Performance Assessment—Viability Assessment (TSPA-VA) to assess waste-package (WP) corrosion, waste-form dissolution, and radionuclide transport in the EBS. Near-field temperatures predicted by this multiscale approach are compared with temperatures predicted by another hybrid-scale (i.e., mountain–drift-scale) modeling approach developed at Lawrence Livermore National Laboratory (LLNL).

This study focused on hydrologic parameters that are found to affect near-field and EBS TH conditions. Parameters found to be of key importance fall under three categories:

1. **Matrix parameters** govern the matrix imbibition diffusivity D_{imb}, which is an index of the tendency for rewetting by flow in the tuff matrix: rock dryout, *RH* reduction, and temperature increase in the near field decrease strongly with increasing D_{imb} of the local host-rock unit.
2. **Fracture parameters** govern the magnitude of capillary wicking in fractures: the van Genuchten alpha parameter α_f for fractures and the fracture permeability (which, for the host-rock units, is well quantified using the bulk permeability k_b). The magnitude of capillarity increases with decreasing α_f. Because the rewetting flux by capillary wicking in fractures increases with capillarity, rock dryout, *RH* reduction, and temperature increase in the near field increase with α_f of the local host-rock unit.
3. **Nonequilibrium fracture–matrix interaction** is strongly affected by the fracture–matrix interaction (FMX) parameter, which is used in the dual-permeability method (DKM) to account for the channeling of flow as the liquid phase "fingers" through the fracture network. Because the tendency for condensate shedding increases with decreasing FMX, rock dryout, *RH* reduction, and temperature increase in the near field tend to increase with decreasing FMX of the local host-rock unit.

Of these three categories, the first category (D_{imb}) is found to have the strongest influence on near-field and EBS TH conditions. For the tsw36 (Tptpln) host-rock unit, there are large differences in the value of D_{imb} between the TSPA-VA hydrologic parameter sets and alternative hydrologic parameter sets that have been developed on the basis of TH analyses of the Large-Block Test (LBT) and Single-Heater Test (SHT). The hydrologic properties of tsw36 unit in the November 1997 TH parameter set and in the December 1997 modified-TH parameter set give much better agreement with the temperatures measured in those field tests. The November 1997 TH parameter set and the December 1997 modified-TH parameter set result in greater rock dryout, *RH* reduction, and temperature increase than do the July 1997 TSPA-VA preliminary base-case parameter set and the December 1997 TSPA-VA base-case parameter set. The differences among these parameter sets is greatest on the western side of the repository where the drifts reside in the tsw36 host-rock unit.

A comparison is made of the near-field temperatures predicted by the multiscale TH model used in this study and the LBNL east–west cross-sectional TH model for the December 1997 TSPA-VA base-case I x 1 $\alpha_{f,mean}$ parameter set. At the center of the repository, the two models predict very similar boiling-period duration. At a location close to the western edge

of the repository, the LBNL model predicts a longer boiling-period duration than is predicted by the LLNL model. The primary cause of this difference is that the edge location in the LBNL model is further removed from the edge of the repository heated footprint than it is in the LLNL model. During the post-boiling period, the temperatures predicted by the two models are in close agreement.

Because of its coarser grid-block discretization, the LBNL model does not capture the early-time near-field temperature buildup that is predicted by the LLNL model during the first 10 yr. For some period thereafter, both models predict high-temperature, superheated conditions at both the center and edge locations in the repository. Because of a larger assumed areal power density (APD), the LBNL model predicts higher peak temperatures than does the LLNL model. Because of its coarser lateral grid-block discretization (i.e., the direction perpendicular to the drift axis), the LBNL model underpredicts condensate shedding between drifts. Consequently, the LBNL model predicts more condensate buildup above the repository horizon than is predicted by the LLNL model. The greater condensate buildup predicted by the LBNL model results in more unstable TH behavior—with a rapid transition from superheated conditions to heat-pipe conditions, which is followed by a second period of superheated conditions at the repository-center location. The peak temperature during the second superheated period in the LBNL model corresponds almost exactly with the temperature predicted in the LLNL model, indicating that the LBNL model has a tendency of predicting a rock dryout extent that is similar to that predicted by the LLNL model. The second superheated period in the LBNL model is followed by another abrupt transition to heat-pipe conditions that persist until the end of the boiling period.

The general agreement between the two models is promising. If the lateral grid-block discretization in the LBNL model were increased to be comparable with that used in the LLNL model and if identical thermal-loading conditions were applied to both models, it is possible (and perhaps likely) that the temperatures predicted by the two models would be in very good agreement. It would be useful to continue the benchmarking exercises between the two modeling approaches. In future comparisons, it would also be useful to include comparisons of liquid-phase saturation, relative humidity, and liquid-phase flux above the drift.

5. References

Bahney, R.H. (1997). *Preliminary Design Basis for WP Thermal Analysis.* (DI #BBAA00000-01717-0200-00019, Rev. 00) Las Vegas, NV: Civilian Radioactive Waste Management System, Management and Operating Contractor. [MOL.19980127.0718]

Bodvarsson, G.S., and T.M. Bandurraga (1996). *Development and Calibration of the Three-Dimensional Site-Scale Unsaturated Zone Model of Yucca Mountain, Nevada.* Berkeley, CA: Lawrence Berkeley National Laboratory, Earth Sciences Division. [MOL.19970211.0176]

Bodvarsson, G.S., T.M. Bandurraga, and Y.S. Wu (1997). *The Site-Scale Unsaturated Zone Model of Yucca Mountain, Nevada, for the Viability Assessment.* June, 1997. (LBNL-40376, UC-814) Berkeley, CA: Lawrence Berkeley National Laboratory, in collaboration with the U.S. Geological Survey. [MOL.19971014.0232]

Buesch, D.C., R.W. Spengler, T.C. Moyer, and J.K. Greslin (1995). *Revised Stratigraphic Nomenclature and Macroscopic Identification of Lithostratigraphic Units of the Paintbrush Group Exposed at Yucca Mountain, Nevada.* Open-File Report. (OFR 94-469) Denver, CO: U.S. Geological Survey. [MOL.19960702.0036]

Buscheck, T.A. (1996). "Hydrothermal Modeling (Section 1.0)." D.G. Wilder, ed. *Near-Field and Altered-Zone Environment Report (Volume II).* Livermore, CA: Lawrence Livermore National Laboratory. (UCRL-JC-124998) [MOL.19961212.0122]

Buscheck, T.A. (1997). *Analysis of Thermal-Hydrological Behavior During the Heating Phase of the Single-Heater Test at Yucca Mountain.* Milestone report for the CRWMS Management and Operating Contractor, U.S. Department of Energy. (SP9266M4) Livermore, CA: Lawrence Livermore National Laboratory. [MOL.19980109.0241]

Buscheck, T.A., J. Gansemer, T. DeLorenzo, J.J. Nitao, R.J. Shaffer, M.J. Cordery, and K.H. Lee (1997). *Thermal-Hydrological Models of the Distribution of Temperature, Relative Humidity, and Gas-Phase Air-Mass Fraction in Repository Drifts.* Milestone report for the CRWMS Management and Operating Contractor, U.S. Department of Energy. (SPLD1M4 and SPLD2M4) Livermore, CA: Lawrence Livermore National Laboratory. [MOL.19980109.0248]

Buscheck, T.A., and J.J. Nitao (1994). *The Impact of Buoyant Gas-Phase Flow and Heterogeneity on Thermo-Hydrological Behavior at Yucca Mountain.* (UCRL-JC-115351) Livermore, CA: Lawrence Livermore National Laboratory. [NNA.19940524.0009]

Buscheck, T.A., J.J. Nitao, and L.D. Ramspott (1996). "Near-Field Thermal-Hydrological Behavior for Alternative Repository Designs at Yucca Mountain." W.J. Gray and I.R. Triay, eds. *Scientific Basis for Nuclear Waste Management XX.* Materials Research Society Symposium Proceedings 465. Warrendale, PA: Materials Research Society. (Also UCRL-JC-124629, Lawrence Livermore National Laboratory, Livermore, CA) [MOL.19961014.0031]

CRWMS M&O (1998). *Total System Performance Assessment—Viability Assessment Technical Basis Document: Chapter 3, Volume 2.* (B00000000-01717-4301-00003, Rev. 0) Las Vegas, NV: prepared by the Civilian Radioactive Waste Management System,

Management and Operating Contractor, TRW Environmental Safety Systems, Inc.

Flint, A., J.A. Hevesi, and L.E. Flint (1996a). *Conceptual and Numerical Model of Infiltration for the Yucca Mountain Area, Nevada.* Water Resources Investigation Report. (3GUT623M) Denver, CO: U.S. Geological Survey. (U.S.G.S. Survey Milestone Report) [MOL.19970409.0087]

Flint, L.E., A.L. Flint, C.A. Rautman, and J.D. Istok (1996b). *Physical and Hydrologic Properties of Rock Outcrop Samples at Yucca Mountain, Nevada.* Open File Report. (95-280) Denver, CO: U.S. Geological Survey. [225884]

Francis, N.D., C.K. Ho, and M.T. Itamura (1997). *UZ-Thermohydrology: Complete VA T/H Sensitivity Analysis.* (SLX09F9) Albuquerque, NM: Sandia National Laboratories. [MOL.19980210.0914]

Hardin, E.L., S.C. Blair, T.A. Buscheck, D.A. Chesnut, L.D. DeLoach, W.E. Glassley, J.W. Johnson, R.B. Knapp, K. Lee, A. Meike, K. Myers, J.J. Nitao, C.E. Palmer, L.L. Rogers, N.D. Rosenberg, B.E. Viani, H.F. Wang, C. Wittwer, and T.J. Wolery (1998). *Near-Field/Altered-Zone Models Report.* Milestone report for the CRWMS Management and Operating Contractor, U.S. Department of Energy. (UCRL-ID-129179) Livermore, CA: Lawrence Livermore National Laboratory.

Haukwa, C., Y.S. Wu, J.J. Hinds, W. Zhang, A.C. Ritcey, L.H. Pan, A.M. Simmons, and G.S. Bodvarsson (1998). *Results of Sensitivity Studies of Thermo-Hydrologic Behavior Conducted on Hydrologic Parameter Sets.* July 31, 1998. Milestone report for the CRWMS Management and Operating Contractor, U.S. Department of Energy. (SP3CK5M4) Berkeley, CA: Lawrence Berkeley National Laboratory.

Ho, C.K. (1997). "Models of fracture-matrix interactions during multiphase heat and mass flow in unsaturated fractured porous media." In proceedings from *1997 ASME International Mechanical Engineering Congress and Exposition.* Dallas, TX. ASME Fluids Engineering Division. [MOL.19971125.0236]

Nitao, J.J. (1988). *VTOUGH—An Enhanced Version of the TOUGH Code for Thermal and Hydrologic Simulation of Large-Scale Problems in Nuclear Waste Isolation.* (UCID-21954) Livermore, CA: Lawrence Livermore National Laboratory. [NNA.19900508.0040]

Nitao, J.J. (1991). "Theory of matrix and fracture flow regimes in unsaturated, fractured porous media." In proceedings from *Second International High-Level Radioactive Waste Management Conference.* Las Vegas, NV: April 28–May 3, 1991. La Grange Park, IL: American Nuclear Society. (Also UCRL-JC-104933, Lawrence Livermore National Laboratory, Livermore, CA) [NNA.910523.0117; 234964]

Nitao, J.J. (1995). *Reference Manual for the NUFT Flow and Transport Code, Version 1.0.* Livermore, CA: Lawrence Livermore National Laboratory. (UCRL-IC-113520)

Zimmerman, R.W., and G.S. Bodvarsson (1989). "An approximate solution for one-dimensional absorption in unsaturated porous media." *Water Resources Res.* **25**(6):1422–1428. [221942]

Technical Information Department • **Lawrence Livermore National Laboratory**
University of California • Livermore, California 94551